Reversible One-way Lipid Transfer at ER-Autophagosome Membrane Contact Sites via Atg2

Li Hao[1], Tomoki Midorikawa[1], Yuta Ogasawara[4], Takuma Tsuji[4], Takuma Kishimoto[5], Yutaro Hama[4], Huichao Lang[1], Nobuo N. Noda[4], Kuninori Suzuki[1,2,3,*]

[1]Department of Integrated Biosciences, Graduate School of Frontier Sciences, The University of Tokyo, Kashiwa, Japan

[2]Collaborative Research Institute for Innovative Microbiology, The University of Tokyo, Tokyo, Japan

[3]Life Science Data Research Center, The University of Tokyo, Kashiwa, Japan

[4]Institute for Genetic Medicine, Hokkaido University, Sapporo, Japan.

[5] Department of Integrative Life Sciences, Graduate School of Life Sciences, Tohoku University, Sendai, Japan

*Corresponding author: Kuninori Suzuki, kuninori@k.u-tokyo.ac.jp

Keywords: Atg2, autophagosome formation, bridge-like lipid transport, *in vivo* observation, lipid dynamics, membrane contact sites

Abbreviations

ARS, autophagy-related structure; Cryo-EM, cryo-electron microscope; DOPE, 1,2-dioleoyl-sn-glycero-3-phosphoethanolamine; ER, endoplasmic reticulum; ERES, ER exit site; FRAP, fluorescence recovery after photobleaching; GFP, green fluorescent protein; IM, isolation membrane; LTP, lipid transfer protein; mApe1, mature Ape1; MCS, membrane contact site; MD, molecular dynamics; MEF, mouse embryonic fibroblasts; mNG, monomeric NeonGreen; ORP, oxysterol-binding protein-related protein; OSBP, oxysterol-binding protein; OSW-1, orsaponin; PAS, pre-autophagosomal structure/phagophore assembly site; PE, phosphatidylethanolamine; PI(3)P, phosphatidylinositol 3-phosphate; PM, plasma membrane; POPC, 1-palmitoyl-2-oleoyl-glycero-3-phosphocholine; prApe1, precursor Ape1; PS, phosphatidylserine; R18, octadecyl rhodamine B; RBG, repeating β-groove; WT, wild-type.

Abstract

Bridge-like lipid transfer proteins (LTPs) contain a repeating β-groove domain and long hydrophobic grooves that act as bridges at membrane contact sites (MCSs) to efficiently transfer lipids. Atg2 is one such bridge-like LTP essential for autophagosome formation, during which a newly synthesized isolation membrane (IM) emerges and expands through lipid supply. However, studies on Atg2-mediated lipid transfer are limited to *in vitro* studies due to the lack of a suitable probe for monitoring phospholipid dynamics *in vivo*. Here, we characterized the lipophilic dye octadecyl rhodamine B (R18), which internalizes and labels the endoplasmic reticulum (ER) in a manner that requires flippases and oxysterol-binding protein–related proteins. Using R18, we demonstrated phospholipid transfer from the ER to the IM during autophagy *in vivo*. Upon autophagy termination, we observed reversible phospholipid flow from the IM to the ER in response to environmental changes. Our findings highlight the critical role of bridge-like LTPs in MCS-mediated phospholipid homeostasis.

Introduction

Phospholipids are key constituents of various organelle membranes in eukaryotic cells. They are regulated asymmetrically and heterogeneously to form permeability barriers that separate organelles from their surroundings, creating distinct compartments. This organization facilitates the segregation and regulation of numerous reactions within cells. Cells maintain lipid homeostasis in organelle membranes by actively translocating and transferring lipids, ensuring optimal membrane function.

Membranes exchange phospholipids with each other via vesicular and nonvesicular pathways. In vesicular trafficking, vesicles transport lipids through secretory and endocytic pathways[1]. However, this process has several limitations. First, the quantity and rate at which vesicles deliver lipids are insufficient for organelle biogenesis[2]. Second, lipid transfer occurs in organelles that do not receive vesicles[3]. Therefore, it is plausible that pathways involved in the transport of phospholipids via mechanisms other than vesicular transport are crucial for maintaining cellular functions[4-7]. Nonvesicular trafficking primarily relies on lipid transfer proteins (LTPs) at membrane contact sites (MCSs), where the two organelles physically interact. Lipid transfer at these sites typically affects the functions of either organelle alone or both organelles[8-10]. The most well-characterized LTPs have a box-like structure with a hydrophobic core, allowing them to hold one or a few lipids[10-12]. These proteins transport lipids by first docking onto the donor membrane, extracting specific lipids. They diffuse through the cytoplasm before inserting the lipids into the acceptor membrane[10, 13]. Recent studies have identified a new class of bridge-like LTPs characterized by repeating β-groove (RBG) domains and extended hydrophobic grooves[14, 15]. These large structures allow LTPs to bridge MCSs and facilitate efficient lipid transfer[7]. Five RBG proteins—Vps13, Atg2, BLTP1 (Tweek/Csf1/KIAA1109), BLTP2 (Hob/Fmp27/KIAA0100), and BLTP3 (SHIP164)[15-24]—have been identified in eukaryotes.

Among the bridge-like LTPs, Atg2 plays a critical role in macroautophagy (herein referred to as autophagy) while Vps13 has been proposed to exhibit a parallel function[25-27]. Autophagy is a universally conserved intracellular degradation pathway that plays an essential role in cell homeostasis and stress responses[28]. It relies on the reorganization of lipid membranes to form an isolation membrane (IM), also known as the phagophore, between the endoplasmic reticulum (ER) and vacuole, which contains engulfed cytoplasmic components. The IM then closes to become an autophagosome, enclosing damaged organelles or protein aggregates for degradation in vacuoles or lysosomes[29-31]. A substantial number of phospholipids is transported to support autophagosome biogenesis, and recent studies have further highlighted the crucial roles of *de novo* phospholipid synthesis in facilitating IM expansion[32-34]. Atg2 forms a complex with Atg18 and the scramblase Atg9 at the edge of the expanding IM during autophagosome formation[35-38]. Atg2-Atg18 complex also constricts IM rims in a phosphatidylinositol 3-phosphate (PI(3)P) dependent manner, promoting autophagosome closure[39]. Additionally, ER exit sites (ERES) have been suggested as a key hub for Atg2 localization during autophagosome biogenesis[40, 41]. Previous *in vitro*

studies on the crystal structure of Atg2 N-terminus suggest that it directly participates in phospholipid transfer at the ER–IM MCS[18]. However, the organelles responsible for the lipid supply for IM expansion are uncertain[42-46].

Considerable progress has recently been made in our understanding of nonvesicular lipid transport. Most evidence supporting the Atg2-mediated lipid transfer model is largely based on *in vitro* studies[17, 18, 25, 47, 48]. However, significant gaps remain in our understanding of direct lipid transfer in living cells. The lack of tools for determining lipid transfer in living cells raises concerns about the validity of conclusions drawn from such studies in a real cellular environment. Additionally, the directionality of lipid transfer by Atg2 remains unclear *in vivo.*

In this study, to investigate lipid transfer during autophagosome formation, we first identified the lipophilic dye octadecyl rhodamine B (R18), which undergoes nonvesicular transport from the plasma membrane (PM) through the ER to autophagy-related structures (ARSs), including the pre-autophagosomal structure/phagophore assembly site (PAS), IMs, autophagosomes, and autophagic bodies. Given that special intracellular transfer route of R18, we investigated lipid transfer from the ER to the IM during autophagosome formation. Our time-lapse imaging analysis also revealed rapid lipid supply accompanied by IM expansion. Our study demonstrated lipid transfer from the ER to the IM and strongly supported the hypothesis that the ER is the primary source of lipids for IM expansion. Furthermore, we developed a repletion assay using a nutrient-rich medium to terminate autophagy under the fluorescence microscope. We identified reversed lipid transfer from the IM to the ER by measuring the recovery of R18 fluorescence at the ER–IM MCS after photobleaching. These findings indicate a reversible one-way lipid transfer mediated by Atg2 at the ER–IM MCS in response to environmental changes. Our research provides direct *in vivo* evidence of the reversible lipid transfer mediated by the bridge-like LTP Atg2, offering new insights into the dynamic regulation of lipid homeostasis during autophagy.

Results

R18 stains the ER and each autophagy-related membrane structure

R18 is a lipophilic fluorescent dye with an alkyl tail composed of 18 carbon atoms, allowing it to be easily inserted into phospholipid membranes. In the last century, it was used to stain membranes in *in vitro* assays; however, its use was gradually phased out with the development of a series of fluorescently labeled phospholipids[49, 50]. We assessed the ability of R18 to label ARSs by performing colocalization analysis using yeast cells expressing Atg8, a marker of ARSs, tagged with mNeonGreen (mNG). mNG–Atg8 was visualized as a distinct dot corresponding to the PAS in wild-type (WT) cells (Figure 1A and 1B). In contrast, R18 signal was not recognized at the mNG-Atg8 labeled dots in *atg2*Δ cells (Figure 1A and 1B). The Atg2–Atg18 complex is absent in the PAS of *atg2*Δ cells[38]. Besides, R18 accumulates at the PAS in Atg8^{G116} *atg4*Δ cells, where the IM fails to expand but Atg2 is still recruited[51]. Taken together, these results suggest that the Atg2–Atg18 complex is involved in the staining of the PAS with R18. Because the IM appears as a dot in WT cells, we enlarged it into a cup-shaped structure by overexpressing prApe1, a selective autophagy cargo (see Figure 4B)[40]. We found that mNG–Atg8 labeled a cup-shaped IM and colocalized with R18 (Figure 1A), as previously reported[51]. We then used the W303 background cells to examine whether a ring-shaped autophagosome could be stained with R18[41]. We found that R18 was colocalized with ring-shaped autophagosomes (Figure 1A and 1B). These data collectively demonstrate that R18 is a fluorescent dye capable of *in vivo* labeling of IMs and autophagosomes.

The outer membrane of the autophagosome fuses with the vacuolar membrane. The inner membrane compartment, referred to as the autophagic body, is then released into the vacuolar lumen and degraded[52]. Here, we examined whether the autophagic body was labeled with R18. We found that mNG–Atg8 diffused throughout the vacuolar lumen of WT cells, representing the disintegration of autophagic bodies (Figure 1C and 1D). Conversely, the vacuolar lumen was not stained with mNG–Atg8 in *atg2*Δ cells (Figure 1C and 1D). Atg15 and Pep4 are crucial vacuolar hydrolases for the breakdown of autophagic bodies[53-55]. In *atg15*Δ and *pep4*Δ cells, the mNG–Atg8-labeled autophagic bodies were found to accumulate inside the vacuole and colocalized with R18, indicating that R18 can label autophagic bodies (Figure 1C and 1D). We also combined *atg15*Δ or *pep4*Δ with *atg1*Δ, which completely blocks autophagosome formation. As expected, mNG–Atg8-labeled autophagic bodies did not accumulate inside the vacuole in these double mutants. R18 showed no vacuolar accumulation (Fig. S1A). These results demonstrate that R18 does not enter the vacuole independently of autophagic bodies delivery.

In Figure 1C, we pre-stained cells with R18 and then induced autophagy by rapamycin treatment, resulting that R18 localized to the ER was transferred to autophagic bodies. We then first induced autophagy by rapamycin treatment and then stained cells with R18. Although mNG–Atg8–positive autophagic bodies accumulated in the vacuole,

R18 staining of the autophagic bodies was not recognized (Fig. S1B). These findings suggest that R18 cannot stain autophagic bodies by diffusion but by autophagy.

ER-phagy is a type of selective autophagy in which the ER is specifically sequestered within autophagosomes and then degraded[56-58]. Because R18 also stains the ER, the dots visualized with R18 could be R18-labeled ER engulfed into autophagic bodies. We used ER-phagy-deficient cells to exclude this possibility. Atg39 and Atg40 localize to the ER membrane, where they participate in the ER-phagy-dependent degradation of the perinuclear and cortical ER, respectively[58]. The *atg39*Δ *atg40*Δ cells exhibited diffusion of mNG within the vacuole (Figure 1E and 1F), indicating that autophagosomes lacking the ER were transported into the vacuole. In *atg15*Δ or *atg15*Δ *atg39*Δ *atg40*Δ cells, we observed the accumulation of mNG-Atg8-labeled autophagic bodies inside the vacuole (Figure 1E and 1F), suggesting the inhibition of autophagic body degradation. Consistently, we found an accumulation of R18-positive autophagic bodies in these cells (Figure 1E and 1F). To further ensure that R18 puncta were not derived from any selective autophagy pathway, we also analyzed *atg11*Δ *atg39*Δ *atg40*Δ cells, in which all forms of selective autophagy are blocked. In this background, mNG–Atg8 labeled puncta still colocalized with R18, confirming that R18 labels the limiting membrane of autophagic bodies independently of selective autophagy (Figure S1C). Together, these results suggest that the limiting membranes of autophagic bodies are labeled with R18. We conclude that R18 can serve as a traceable marker for the membrane dynamics of each ARS, including the PAS, IMs, autophagosomes, and autophagic bodies.

We further validated the localization of R18 by examining its colocalization with green fluorescent protein (GFP)-tagged organelle marker proteins (Figure S2A). We first used FM4-64, which can stain each compartment along the endocytosis pathway and localize to the vacuolar membrane, to validate our method (Figure S2B and S2C). Subsequently, cells expressing GFP-tagged organelle marker protein-expressing cells were stained with R18. We found that R18 colocalized with the ER membrane marker proteins Dpm1-GFP, Erd2-GFP, and Sec61-GFP, which have distinct subcellular localizations (Figure S2D and S2E). R18 colocalized with these ER markers (Figure S2D and S2E). R18 occasionally labeled the vacuolar membrane, possibly due to the fusion of autophagosomes with the vacuole. However, R18 did not colocalize with other organelle markers (Figure S2D and S2E), indicating that it primarily stains the ER.

Finally, we confirmed whether R18 can be used in mammalian cells by testing it in mouse embryonic fibroblasts (MEFs) expressing GFP-tagged ER marker proteins. Under normal conditions, GFP and R18 exhibited clear colocalization following R18 staining (Figure 1G). After starvation-induced autophagy, we found that R18 colocalized with GFP-LC3, an autophagosome marker (Figure 1H). Cross-sectional imaging confirmed that R18 colocalized with GFP-LC3 in the XY and XZ planes, indicating the suitability of R18 for studying autophagy in mammalian cells (Figure 1H). In mammalian cells, the ER is closely associated with the IM. Thus, it is difficult to

distinguish the IM from the ER using fluorescence microscopy. To directly determine whether R18 integrates into autophagosomal membranes, we used freeze-fracture replica electron microscopy, a high-resolution method that preserves membrane phospholipids in a metal–carbon replica[59]. Using this approach, we performed double immunogold labeling of R18 and GFP–LC3. Small (6 nm) gold particles marking R18 and larger (12 nm) particles marking GFP–LC3 were both detected on the autophagosomal membrane, demonstrating that R18 indeed integrates into autophagosomal membranes in starved MEFs (Figure 1I).

Internalization of R18 depends on flippases at the plasma membrane

To further validate R18 as a reliable probe for tracing biologically regulated lipid transfer — rather than passive diffusion — we next examined its intracellular entry pathway. First, we investigated how R18 enters cells and stains the ER, comparing it to the internalization pathway of the well-established lipophilic dye FM4-64[60]. In contrast to FM4-64, which localizes to endocytic compartments, R18 preferentially stains the ER and ARSs (Figures. 1 and S2). These results suggest that FM4-64 and R18 are internalized and transported via different pathways. FM4-64 is internalized via endocytosis, which depends on physiological temperature and ATP[60]. Here, we examined whether biological processes also influence the internalization of R18. We expressed GFP-tagged Dpm1 as a marker of ER transmembrane proteins. At 30°C, cells displayed clear colocalization of R18 with Dpm1-GFP, which preferentially stained the ER (Figure 2A and 2B). However, at 4°C, a drastic accumulation of R18 on the PM was observed (Figure 2A and 2B), suggesting that the internalization of R18 is temperature-dependent. Next, ATP depletion was achieved by inhibiting ATP synthesis through oxidative respiration and glycolysis using NaN_3 and NaF, respectively[61]. Without these inhibitors, R18 colocalized with the ER containing Dpm1-GFP (Figure 2C–2E). However, in the presence of these inhibitors, R18 accumulated on the PM, forming a distinct circular pattern (Figure 2D and 2E). We then washed out NaN_3 and NaF using fresh medium (Figure 2C) and found that R18 rapidly entered the cells, colocalizing with Dpm1-GFP within 3 min (Figure 2D and 2E). This observation indicates the rapid transfer of R18 from the outside of cells to the ER. These results demonstrate that R18 internalization depends on physiological temperature and ATP.

Based on the above results, we hypothesized that flippase is involved in the internalization of R18. Flippase is a type 4 P-type ATPase (P4-ATPase) that catalyzes the translocation of phospholipids from the extracellular leaflet to the cytoplasmic leaflet[62]. Budding yeast exhibit five P4-ATPases (Drs2, Dnf1, Dnf2, Dnf3, and Neo1) that form heterodimeric complexes with noncatalytic subunits of three Cdc50 family member proteins, namely, Cdc50, Lem3, and Crf1[63, 64] (Figure 2F). Among them, Drs2, Dnf1/Dnf2, and Dnf3 form complexes with Cdc50, Lem3, and Crf1, respectively. *Neo1* is an essential gene by itself[65]. Therefore, the phenotypes observed in P4-ATPase-deficient cells should be copied to those observed in cells lacking its subunits [63, 66]. We examined R18 localization in flippase-defective cells. ER staining was defective in *drs2*Δ cells, consistent with the pattern observed in *cdc50*Δ cells, which lack the β-

248 subunit of the P4-ATPase flippase complex. R18 staining was restricted to the PM as
249 discrete dots (Figure 2G and 2H). Furthermore, Neo1-defective cells exhibited a
250 distinct circular pattern, suggesting that R18 is blocked at the PM (Figure 2G and 2H).
251 Quantification of the different patterns revealed a significant difference, suggesting that
252 the Drs2, Cdc50 or Neo1 plays crucial roles in the internalization of R18 (Figure 2I).
253 Notably, Drs2, Cdc50 or Neo1 are required to establish plasma membrane
254 phosphatidylserine (PS) / phosphatidylethanolamine (PE) asymmetry[67]. Our recent
255 study also showed that R18 is blocked at the PM in PE-deficient yeast cells (*psd1*Δ
256 *psd2*Δ)[68]. This defect may be caused by the loss of PE asymmetry at the PM by the
257 defects in Drs2, Cdc50 or Neo1[67].
258
259 Considering that R18 labels ARSs, we hypothesized that the absence of flippase would
260 result in functional defects in autophagy. To test this hypothesis, we performed the
261 GFP–Atg8 processing assay. A centromeric plasmid expressing GFP–Atg8 was
262 transformed into the WT cells, *atg1*Δ cells (the negative control), and each flippase-
263 deficient cell line. Samples were collected and analyzed by western blotting using
264 GFP-specific antibodies. The significant increase in free-GFP levels in WT cells
265 represents the normal progression of autophagy (Figure 2J and 2K). The processing
266 of GFP–Atg8 in *lem3*Δ, *drs2*Δ, *cdc50*Δ, *dnf3*Δ, *crf1*Δ, and Neo1-defective cells was
267 identical to that in the WT cells, indicating that the flippases are not essential for
268 autophagy (Figure 2J and 2K).
269
270 We also investigated selective autophagic activity using the Ape1 maturation assay. In
271 selective autophagy, the precursor Ape1 (prApe1) forms oligomers, which are
272 transported from the cytoplasm into a vacuole and processed into mature Ape1
273 (mApe1)[38]. Both prApe1 and mApe1 were detected using western blotting. Each
274 flippase-defective cell line, but not *atg1*Δ cells, exhibited processing ability comparable
275 to WT cells (Figure 2L and 2M), suggesting that selective autophagic activity was
276 normal in flippase-defective cells. These findings indicate that flippase does not affect
277 autophagy.
278
279 **Transfer of R18 from the PM to the ER depends on the oxysterol-binding protein**
280 **(OSBP)-related proteins (ORPs)**

281 To investigate how R18 is transported from the PM to the ER, we first examined the
282 contribution of tethers at the PM–ER MCS[69]. R18 localized to the ER in tetherΔ cells
283 and colocalized with the ER marker Sec61–GFP (Figure S3A). We then constructed a
284 "super tetherΔ" strain by combining *ice2*Δ with tetherΔ. Even in this background, R18
285 still colocalized with the ER marker Scs2–GFP (Figure 3A), indicating that the transfer
286 of R18 from the PM to the ER does not depend on PM–ER tethers. We noticed that
287 FM4-64 is internalized through endocytosis in 10–15 min[60]. In contrast, our results
288 revealed a rapid transfer of R18 from the PM to the ER in <3 min (Figure 2D). This
289 transfer time is consistent with the time taken for phospholipid transfer by LTPs at the
290 PM–ER membrane contact sites[70, 71]. Furthermore, unlike FM4-64, which primarily
291 stains the organelles in the endocytosis pathway, R18 stains only the ER and ARSs.

We hypothesized that the transfer of R18 from the PM to the ER was carried out by LTPs at the PM–ER MCS.

OSBP ORPs are phospholipid transfer proteins localized to MCSs[72]. In yeast, seven homologs (Osh1–Osh7) mediate nonvesicular sterol transport at the PM–ER MCS[72]. We examined several Osh deletion cells, including *osh3*Δ, *osh1*Δ *osh2*Δ, *osh4*Δ *osh5*Δ, and *osh6*Δ *osh7*Δ. Because deletion of *OSH1-7* is lethal to cells, we used cells harboring the temperature-sensitive allele *osh4-1* in combination with deletions of the other six *OSH* genes (*osh*Δ *osh4-1*). These cells grow at the permissive temperature of 25°C but not at the nonpermissive temperature of 37°C. R18 displayed normal ER localization in WT cells, whereas no notable defects in R18 localization were observed in Osh deletion cells (Figure S3B). But R18 showed partially the PM pattern in *osh1*Δ *osh2*Δ, *osh6*Δ *osh7*Δ, and *osh*Δ *osh4-1* cells (Figure S3B). These results suggest that the transport of R18 from the PM to the ER might be impaired in these strains. Thus, we used orsaponin (OSW-1), a natural compound known to inhibit OSBP function[73, 74], to further validate the role of OSBP in R18 transport. Treatment with OSW-1 caused a noticeable increase in the proportion of cells exhibiting partial PM-localized R18 patterns in Osh deletion cells (Figure 3B–3D). In the temperature-sensitive *osh1-7*Δ *osh4-1* cells, R18 displayed a clear circular pattern on the PM under restrictive conditions (37°C), indicating a complete block in its transport to the ER (Figure 3B–D).

Given that R18 exhibited the same clear circular pattern in Neo1-defective cells, we hypothesized that R18 would remain on the outer leaflet of the PM in Neo1-defective cells and accumulate on the inner leaflet of the PM in OSBP-defective cells. To examine the localization of R18, we treated WT, Neo1-defective, and OSBP-defective cells with sodium dithionite to quench the fluorescence of R18 exposed to the extracellular environment (Figure 3E). We observed no discernible difference in R18 intensity in the ER of WT cells. However, compared with the stable R18 intensity at the PM of OSBP-defective cells, the R18 intensity at Neo1-defective cells decreased significantly (Figure 3F and 3G). This result indicates that R18 remained on the extracellular leaflet and was not internalized in Neo1-defective cells. In contrast, the clear circle pattern on the PM observed in OSBP-deficient cells indicates that R18 accumulates on the cytoplasmic leaflet of the PM and fails to be transferred to the ER. These findings support our hypothesis that flippase and OSBP facilitate R18 transport from the PM to the ER at the PM–ER MCS. Since Neo1- or OSBP-defective cells do not transfer R18 from the PM to the ER, we included these strains as controls to assess the ER dependency of R18 transport to ARSs. In both cells, R18 remained at the plasma membrane and failed to label ARSs, whereas mNG–Atg8 puncta still formed (Figure S3C). These results suggest that R18 must reach the ER before being delivered to ARSs.

Phospholipids are transferred from the ER to the IM at the ER–IM MCS via Atg2

Autophagosome formation requires a constant supply of phospholipids. For several decades, the source of the lipids essential for autophagosome formation has been a

central and longstanding enigma in the field of autophagy. Previous *in vitro* studies suggested that Atg2 acts as an LTP[16, 18, 26, 27]. Moreover, Atg2 localizes between the ER and IM[40, 41]. Therefore, we hypothesized that Atg2 acts as an LTP at the ER–IM MCS (Figure 4A). Despite a recent electron microscopic study highlighting the importance of de novo-synthesized phosphatidylcholine in autophagosome formation[34], direct evidence revealing lipid transfer at the ER–IM membrane contact site in living cells is still lacking, primarily due to the absence of a suitable probe to monitor phospholipid dynamics. Given that R18 stains both the ER and IM (Figure 1), we tried to use R18 as a probe to visualize phospholipid transfer from the ER to the IM *in vivo*.

The IM visualized using mNG–Atg8 appeared as a cup-shaped structure following prApe1 overexpression (Figure 4B). A recent *in silico* study has predicted an Atg2 lipid transfer mutant (*atg2*^{LT}) that the density of phospholipid in the hydrophobic cavity is discontinuous[75]. We constructed the Atg2 lipid transfer mutant. In this mutant, Ape1 maturation was not detected, showing that the process of autophagy is completely blocked, whereas full length Atg2 was expressed (Figure S4A and S4B). In addition, mNG–Atg8 localized adjacent to Sec13–mRuby, suggesting that *atg2*^{LT} mutant can tether ERES and the IM (Figure S4C).

In WT cells, R18 colocalized with mNG-Atg8 as both cup-shaped structures and punctate Atg8 structures (Figure 4C and 4D). In contrast, *atg2*Δ cells showed a dot pattern without R18 as previously reported[51]. Moreover, *atg2*^{LT} cells showed the same pattern with *atg2*Δ cells (Figure 4C and 4D). One group has reported that a phospholipid transfer defective mutant of Atg2 is defective in autophagosome formation[76]. Recently, we have narrowed down the critical loop region of Atg2 and generated the *atg2*Δ21 mutant[77]. This Atg2Δ21 protein is defective in bridge-type lipid transfer activity *in vitro*[77]. R18 staining of mNG-Atg8 labeled structures is also blocked in this mutant *in vivo*[77]. These facts suggest that Atg2^{LT} protein also has a defect in the bridge-type lipid transfer activity. Collectively, these results suggest that the transfer of R18 from the ER to the IM requires the presence of a broad and continuous hydrophobic groove within the bridge-like architecture of Atg2[77].

We next confirmed that R18 stained the IM, as observed under a confocal microscope (Figure 4E). We then performed the fluorescence recovery after photobleaching (FRAP) assay to investigate the dynamics of lipid transfer. We performed photobleaching on both R18 and mNG signals within the expanding IM and monitored their fluorescence recovery (Figure 4F, Supplemental Video 1A-C). The R18 fluorescence recovered rapidly, with a half-recovery time of 10–30 s, suggesting efficient phospholipid transfer from the ER to the IM at the ER–IM MCS (Figure 4F and 4G). Conversely, mNG–Atg8 fluorescence exhibited only limited recovery, suggesting that the supply of Atg8 to the IM during expansion is limited (Figure 4F and 4G). We assume that Atg8 localized at the IM remains essentially constant and the Atg8 pool is used for IM expansion. However, we cannot exclude the possibility that the limited supply of Atg8 is also

important for IM expansion. These findings indicate that phospholipid transfer occurs from the ER to the IM at the ER–IM MCS. Furthermore, the length of the IM at 320 s was increased compared with that at 0 s (Figure 4F and 4H), indicating that the supply of Atg8 to the IM is not required during IM expansion.

Phospholipids are transferred from the IM to the ER after autophagy termination

Although the prApe1 overexpression system enlarged the IM, it can obstruct the formation of a complete autophagosome. Therefore, we focused on the IM when it reached its maximum length during prolonged autophagy (Figure 5A). We performed photobleaching of R18 in a large region encompassing the IM, ER–IM MCS, and adjacent ER areas and subsequently monitored the fluorescence recovery at each area (Figure 5B and 5C, Supplemental Video 2A-C). The IM length did not increase after reaching the maximum length (Figure 5D). The R18 signal at the IM did not recover, indicating that phospholipid transfer from the ER to the IM had ceased (Figure 5C and 5E). We observed a normal recovery curve for R18 at the ER, showing a rapid and distinct recovery. The R18 signal at the ER–IM MCS was expected to recover at a rate comparable to that of the R18 signal at the ER. However, the fluorescence recovery was partial (Figure 5C and 5E). This outcome indicates the possible transfer of phospholipids from the quenched IM to the ER–IM MCS, indicating a previously unrecognized reversed phospholipid flow from the IM to the ER.

To test the possibility of phospholipid transfer from the IM to the ER, we investigated whether this transfer occurs after the termination of autophagy. Cells were subjected to starvation for 4 h in a nitrogen-starvation medium, stained with R18, and seeded onto a glass-bottom dish. Subsequently, autophagy was terminated by replenishing the cells with a nutrient-rich medium, and the cells were examined using time-lapse microscopy (Figure 5F). We then photobleached several regions (the IM / the ER with the ER-IM MCS) to examine phospholipid transfer.

To determine whether nutrient replenishment terminates autophagy, we selectively photobleached the R18 signal and monitored the R18 (photobleached) and mNG–Atg8 (without photobleaching) signal following nutrient replenishment (Figure 5G and 5H, Supplemental Video 3A–C). We observed a marked decrease in the mNG–Atg8 signal (Figure 5G–5I), indicating the dissociation of Atg8 from the IM. Based on this result, we conclude that nutrient repletion terminates autophagosome formation. Next, we photobleached the R18 signal on the IM 80 s after nutrient replenishment (Figure 5H). We observed minimal fluorescence recovery at the IM (Figure 5G and 5H), suggesting that phospholipid transfer from the ER to the IM ceases upon autophagy termination (Figure 5H and 5I). Therefore, the cessation of anterograde lipid transfer is likely accompanied by the termination of autophagosome formation.

Next, we photobleached the ER region and monitored R18 signal recovery at the ER–IM MCS (Figure 5J and 5K, Supplemental Video 4). Time-lapse imaging revealed

gradual dissociation of mNG–Atg8 at the IM after autophagy termination (Figure 5K). Following photobleaching in the ER region, R18 fluorescence was recovered at the ER–IM MCS (Figure 5K). To determine whether the phospholipids at the ER–IM MCS originated from the IM or ER, we generated a fluorescence intensity recovery curve at the ER–IM MCS, normalizing it to the intensity of the unbleached IM or ER region as the background. We observed a significant recovery of R18 fluorescence at the ER–IM MCS when the R18 fluorescence at the ER–IM MCS was normalized to that of the unbleached IM (Figure 5L), suggesting that a portion of the phospholipids in the ER–IM MCS were supplied from the IM following nutrient replenishment. Importantly, consistent with the reversed lipid flow, both Atg2 and Atg18 remained localized at the ER–IM MCS during the nutrient-replenishment assay. Time-lapse imaging showed that the Atg2 and Atg18 persisted at the contact site even after autophagy termination, supporting that the Atg2-Atg18 complex mediates lipid transfer from the IM to the ER during IM shrinkage (Figure S5; Supplemental Video 5).

To further confirm that the recovered fluorescence at the ER–IM MCS originates from the IM rather than the adjacent bleached ER (Figure 5J and 5K), we quantified the recovery of the adjacent bleached ER region. When normalized to unbleached ER, the adjacent bleached ER showed an average recovery 20% lower than that of the ER–IM MCS (28%). Furthermore, we also normalized the recovery to the unbleached IM, the adjacent bleached ER showed a much lower recovery (47%) compared to the ER–IM MCS (80%) (Figure 5L and 5M). These results indicate that at the time when fluorescence recovery at the ER–IM MCS is already apparent, the adjacent ER remains in a slower and weaker recovery phase, supporting that the recovered signal at the ER–IM MCS originates from the IM (Figure 5L and 5M). Taken together, our results indicate that the phospholipids on the IM may be transferred back to the ER during IM shrinkage after autophagy termination. Therefore, our findings provide evidence of reversible one-way lipid transfer at the ER–IM MCS.

To gain insights into the structural properties underlying the Atg2-mediated phospholipid transfer process, we employed the predictive capabilities of AlphaFold3. We modeled a system consisting of 12 molecules of 1-palmitoyl-2-oleoyl-glycero-3-phosphocholine (POPC), 12 molecules of 1,2-dioleoyl-sn-glycero-3-phosphoethanolamine (DOPE), four molecules of R18, and the RBG domain of Atg2 (residues 1–1346). The phospholipids and R18 molecules were aligned in a side-by-side configuration via the RBG domain of Atg2 (Figure 6A). Because of the inability to identify the mechanism governing the directionality of phospholipid transfer, this result suggests that phospholipids can diffuse in either direction. Cellular requirements may regulate the direction of phospholipid transfer at the ER–IM MCS. For instance, phospholipids are transferred from the ER to the IM via Atg2 during autophagosome formation. Conversely, upon autophagy termination, the phospholipid flow appears to be reversed, with the retrieval of phospholipids from the IM to the ER. The present study posits that the ER–IM MCS is a pivotal hub for regulating lipid flux between the IM and ER.

Discussion

The study of MCSs substantially enhanced our understanding of phospholipid transfer, revealing that nonvesicular transport processes facilitate rapid and efficient lipid exchange between organelles. These processes are critical for maintaining cellular homeostasis, especially under stress or nutrient-deprivation conditions. In particular, the recent discovery of bridge-like LTPs has further significantly advanced our understanding of the structural and functional intricacies of phospholipid transfer. Bridge-like LTPs such as Atg2 and Vps13 act as molecular conduits for lipid transport, facilitating the coordinated transfer of lipids across MCSs. Despite significant structural and biochemical research progress, our understanding of lipid dynamics in living cells remains limited. Most of our current knowledge is based on *in vitro* experiments, raising concerns about the translatability of *in vitro* findings in fundamental biological research[78].

A major constraint in our *in vivo* investigation of lipid transfer thus far has been the lack of a probe to monitor phospholipid movement. R18 was initially used to study membrane fusion during viral infection *in vitro* around 1980, coinciding with the establishment of *in vitro* assays. However, this application was subsequently abandoned by approximately 2000[50]. Our group had previously reported that R18 stains the ER[51]. The ER forms various MCSs with other organelles to facilitate lipid exchange via bridge-like LTPs. Among these LTPs, Vps13 localizes to multiple organelles and MCSs, including the ER-mitochondrion and ER-endosome MCSs[23]. R18 specifically stained the ER and occasionally labeled the vacuolar membrane, possibly due to autophagosome–vacuole fusion, but did not stain other organelles (Figure S2). Moreover, our findings indicate that R18 is specifically transferred via Atg2 at the ER–IM MCS (Figure 1 and 4). Our parallel study also confirmed Atg2 is indeed a bridge-like LTP and the transfer of R18 depends on this bridge-type lipid transfer activity at the ER-IM MCS[77]. Therefore, the transfer of R18 mediated by Vps13 and other bridge-like LTPs may be limited due to differences in the structural length and width of their hydrophobic grooves. The regulation of phospholipid transfer in various MCSs may involve a gating function restricting phospholipid transfer.

Our study analyzed phospholipid transfer pathways using R18 from the external environment of cells. In comparison with existing phospholipid traceable probes, such as FM4-64, NBD-PC, and NBD-PE, which are transported via the endocytosis pathway, we have established R18 as a novel probe for tracking lipid transfer through the nonvesicular pathway in living cells. R18 was initially internalized at the plasma membrane in a flippase-dependent manner involving Neo1 and Drs2 (Figure 2). Flippases are a type of phospholipid transporter responsible for maintaining lipid asymmetry[64]. R18 exhibited a distinct circular pattern on the PM in Neo1-defective cells, in contrast to a dot pattern in Drs2 deletion cells, suggesting the presence of entry regions or tethering sites for phospholipid translocation. Neo1 is likely required for R18 to access these entry regions on the PM. However, Neo1 is believed to be involved in recycling processes at the endosome and trans-Golgi network while also

511 playing a role in regulating the PS/PE asymmetry of the PM[67, 79]. Most recently, we
512 further determined that R18 internalization strictly depends on PE in the PM[68]. Our
513 findings provide valuable insights that could inform future mechanistic studies of Neo1.
514 We found no direct relationship between phospholipid flipping and autophagic activity,
515 suggesting that R18 translocation occurs independently of flippase function, even
516 when R18 reaches each ARS.
517
518 Following the treatment of *osh*Δ *osh4-1* cells with OSW-1, an OSBP inhibitor, at a
519 restrictive temperature, R18 displayed a distinct circular blocking pattern (Figure 3).
520 This result indicates the transfer of R18 from the PM to the ER via OSBP. One potential
521 explanation for this phenomenon is that OSW-1 protein strongly inhibits Osh4-1 at the
522 restrictive temperature. An alternative explanation is that undetermined OSBP(s) with
523 low activity levels may exist that are effectively inhibited by OSW-1. Further elucidation
524 of the molecular mechanisms underlying flippase and OSBP function requires more
525 detailed structural studies. FRAP analysis of R18 can also be performed at the PM–
526 ER MCS to investigate phospholipid transfer *in vivo*.
527
528 We demonstrated that R18 labels ARSs in both yeast and mammalian cells (Figure 1).
529 In mammalian cells, the IM is sandwiched between the ER membranes, making it
530 difficult to solely identify the flow of phospholipids within the IM[28]. Therefore, we
531 considered *Saccharomyces cerevisiae* a suitable organism for determining the
532 directions of phospholipid transfer at the ER–IM MCS. A major point of contention in
533 the field of autophagy is the primary phospholipid source for autophagosome
534 formation[80]. Our *in vivo* results strongly support the ER as the main membrane source
535 of phospholipids, which are transferred via Atg2 to the expanding IM (Figure 4).
536
537 To investigate reversible phospholipid transfer, we leveraged the inherent defect of the
538 prApe1 overexpression system as a key tool to enlarge the IM and prevent its closure
539 into a complete autophagosome. We developed a nutrient-rich medium replenishment
540 assay to terminate autophagy and focused on the IM with the maximum length (Figure
541 5). Atg8 dissociation may lead to IM shrinkage since we found gradual dissociation of
542 mNG–Atg8 from the IM and reversed phospholipid flow from the IM to the ER after
543 autophagy termination. Our FRAP data also showed that after the initial dissociation
544 of Atg8, the IM membrane undergoes a relatively slow disassembly process
545 suggesting that Atg8 maybe the trigger for IM shrinkage. Further research employing
546 additional marker proteins for the IM (Atg1 and Atg16-5-12) is essential to
547 comprehensively understand the disintegration process. We also developed a
548 phospholipid transfer model of Atg2 (residues 1–1346) using AlphaFold3[81] (Figure 6A).
549 The side-by-side alignments in the RBG cavities further support our *in vivo* evidence
550 for the reversible one-way lipid transfer via Atg2 at the ER–IM MCS. This finding
551 highlights the critical role of bridge-like LTPs at MCSs in response to dynamic
552 environmental conditions.
553
554 Our *in vivo* evidence demonstrated that reversible phospholipid transfer by Atg2 is a

key mechanism by which cells regulate lipid homeostasis during autophagy induction and termination (Figures. 4–6). These findings also raise intriguing questions, such as how cells regulate millions of phospholipid molecules within minutes, transferring them via bridge-like LTPs at MCSs in response to environmental changes. A major issue not addressed in this study is the driving force for the reversible one-way lipid transfer at the ER–IM MCS via Atg2. Based on our findings, we hypothesized that a driving force acts on donor and receptor organelles. Furthermore, based on the studies of VPS13 in mammalian cells and the role of the Atg2–Atg9 complex in autophagy, we propose that cells regulate phospholipid transfer through a gating function in response to environmental changes. Bridge-like LTPs are likely regulated by other proteins, such as scramblase, localized at both organelles at MCSs. Nevertheless, this study successfully identified a traceable probe for phospholipids undergoing nonvesicular transport and demonstrated reversible, one-way lipid transfer via Atg2 at the ER–IM MCS. This major advancement contributes to our understanding of phospholipid transfer via bridge-like LTPs, which play a role in various cellular functions *in vivo*. Additionally, it provides insights into the chemical and biophysical aspects necessary for developing traceable probes for nonvesicular transport.

572 **Methods**

573 **Yeast strains and media**

574 *The S. cerevisiae* strains and plasmids used in this study are listed in Supplementary
575 Tables 1 and 2, respectively. Cells were cultured in YPD (1% Bacto™ yeast extract, 2%
576 Bacto™ peptone, and 2% glucose), SDCA (0.17% Difco™ yeast nitrogen base w/o
577 amino acids and ammonium sulfate, 0.5% ammonium sulfate, 0.5% Bacto™ casamino
578 acids, and 2% glucose), or SDGA (0.17% Difco™ yeast nitrogen base w/o amino acids
579 and ammonium sulfate, 0.5% ammonium sulfate, 0.5% Bacto™ casamino acids, and
580 2% galactose) supplemented with appropriate nutrients. Plasmid amplification was
581 performed using *Escherichia coli* strain XL1-Blue grown in LB medium (1% Bacto™
582 tryptone, 0.5% Bacto™ yeast extract, and 1% NaCl). Ampicillin was added to the LB
583 medium at 60 μg/mL when relevant. Yeast cells were transformed using the lithium
584 acetate method[82]. The *atg2*^{LT} mutant cells are constructed by the CRISPR/Cas9
585 system provided by Ellis lab (https://benchling.com/pub/ellis-crispr-tools).
586
587 To activate the Cu^{2+}-inducible *CUP1* promoter, cells were cultured for 1 day in a
588 medium containing 250 μM $CuSO_4$ prior to the experiments. Autophagy was induced
589 by transferring cells to nitrogen-starvation SD(−N) medium (0.17% yeast nitrogen base
590 without amino acids and ammonium sulfate, and 2% glucose) or by treating cells with
591 0.2 μg/mL rapamycin (Sigma Aldrich). Standard protocols were used for yeast
592 manipulation[83].
593 The yeast cells were treated with a mixture of NaF and NaN_3 at a final concentration
594 of 10 mM for 5 min. For galactose induction of *Neo1* using the *GAL1* promoter, cells
595 were cultured in SDGA medium supplemented with appropriate nutrients. The
596 following day, the cells were collected and washed three times with an SDCA medium
597 to remove the galactose, initiating the suppression of *Neo1* expression. The cells
598 (OD_{600} = 1.0–2.0) were then resuspended in SDCA medium and incubated for 12 h to
599 suppress *Neo1* expression.
600

601 **Fluorescence microscopy**

602 Cells were cultured overnight, diluted, and then cultured in SDCA medium
603 supplemented with appropriate nutrients until reaching the log phase (~2 × 10^7 cells
604 per mL; OD_{600} = ~1). For R18 staining, cells were incubated with R18 (Invitrogen) at 5
605 μg/mL (from a 1 mg/mL stock dissolved in dimethyl sulfoxide) for 10 min in a nutrient-
606 rich medium at 30 ℃. The cells were then washed thrice with a fresh medium. FM4-64
607 staining was performed as previously described[60].
608 For visualization of IM, cells were cultured in the presence of 250 μM $CuSO_4$ overnight
609 to activate the *CUP1* promoter and induce prApe1 expression. The cells were then
610 diluted and cultured in SDCA medium containing 250 μM $CuSO_4$ until they reached the
611 log phase (~2 × 10^7 cells per mL; OD_{600} = ~1). Fluorescence imaging was performed
612 using an IX83 inverted system microscope (Olympus) equipped with a
613 UPlanSApo100× oil-immersion lens (1.40 NA; Olympus) and a CoolSNAP HQ CCD
614 camera (Nippon Roper). U-HGLGPS (Olympus), a mercury light source system, was
615 used to excite fluorescent proteins. U-FGFP and U-FRFP filter sets (Olympus) were

616 used for GFP and R18 visualization, respectively. Images were acquired using the
617 Micro-Manager software (version 1.4.6, https://micro-manager. org). Samples were
618 prepared on 76×26-mm glass slides (S1225; Matsunami) and 18×18-mm glass
619 coverslips (No. 1-S; Matsunami).
620
621 **Confocal microscopic analysis of mammalian cells**
622 ER (Calreticulin-KDEL-GFP) labeling was performed using CellLight™ ER-GFP,
623 BacMam 2.0 (C10590; Thermo Fisher Scientific). To induce autophagy, MEFs stably
624 expressing GFP-LC3 were cultured in Earle's Balanced Salts (E2888-500ML; Sigma)
625 for 3 h.
626 Live cells seeded in 35-mm glass-bottom dishes (P35G-1.5-14-C; Mattek) were
627 maintained at 37 °C with 5% CO_2 and observed under a Ti2 inverted microscope (Nikon)
628 equipped with a Nikon A1 HD25 (Nikon) confocal system and Plan Apo λ 60x oil-
629 immersion lens (1.4 NA; Nikon). The pinhole size was set to 1.0 Airy units. For 3D
630 imaging, z-stack images were acquired using a Plan Apo λ 60x oil-immersion lens with
631 Galvano scanning using two frame averages, and the pinhole size was set to 0.8 Airy
632 units. The images were captured using NIS-Elements (Nikon). The images of
633 deconvolution were processed using Nikon's original ER deconvolution algorithm.
634
635 **Quick-freezing and freeze-fracture replica labeling**
636 MEF cells were starved for > 2 hours and incubated with 50 μg/mL R18 for 10 min.
637 Cells were detached from the substrate by a brief treatment with trypsin and
638 ethylenediaminetetraacetic acid (EDTA) and pelleted. Copper EM grids (150 mesh,
639 Nisshin EM) were immersed in cell pellet, and sandwiched between a flat aluminum
640 disk (Engineering Office M. Wohlwend, Sennwald, Switzerland) and a thin copper foil
641 (20 μm thick; Nilaco). The specimens were quick-frozen using HPM 010 high-pressure
642 freezing machine according to the manufacturer's instruction (Leica Microsystems,
643 Wetzlar, Germany). The frozen specimens were transferred to the cold stage of
644 ACE900 (Leica Microsystems, Wetzlar, Germany), fractured at −102°C under a
645 vacuum of ~ 1 × 10-6 mbar. Replicas were made by electron-beam evaporation in
646 three steps: carbon (6 nm thick) at an angle of 90º to the specimen surface, platinum-
647 carbon (2 nm thick) at an angle of 45º, and carbon (10 nm thick) at an angle of 90º.
648 Thawed replicas were treated with 2.5% SDS in 0.1 M Tris·HCl (pH 8.0) at 60 °C
649 overnight.
650 For the double labeling of R18 and GFP-LC3, replicas were washed with phosphate-
651 buffered saline (PBS) containing 0.1% Triton X-100 (PBST). After blocking nonspecific
652 sites with 3% bovine serum albumin (BSA) in PBS, the samples were incubated at 4 °C
653 overnight with 60 μg/mL mouse anti-rhodamine B monoclonal antibody (Creative
654 Diagnostics, NY, USA) and 10.4 μg/mL rabbit anti-GFP antibody (provided by Dr
655 Masahiko Watanabe of Hokkaido University) in PBS containing 1% BSA. The samples
656 were then incubated with 20-fold diluted 6 nm colloidal gold AffiniPure goat anti-mouse
657 IgG and 12 nm colloidal gold AffiniPure goat anti-rabbit IgG (Jackson
658 ImmnunoResearch Laboratories, PA, USA) in PBS containing 1% BSA for 60 min at
659 37°C. The labeled replicas were observed with JEOL JEM-1400plus EM (Tokyo,

660 Japan).
661
662 **Confocal microscopic analysis of yeast cells**
663 A confocal laser scanning microscope FV-3000 (Olympus) equipped with a
664 UPLSAPO60XO oil-immersion objective lens (1.42 NA; Olympus) was used. Lasers
665 (488 and 561 nm) were employed for linear sequential excitation, and fluorescence in
666 the ranges of 500–540 nm and 560–600 nm was recorded for mNG and octadecyl
667 rhodamine B (R18; Invitrogen), respectively, using a resonant scanner. Samples were
668 prepared on 76×26-mm glass slides (S1225; Matsunami) and 18×18-mm glass
669 coverslips (No. 1-S; Matsunami). The images were analyzed using ImageJ
670 (https://fiji.sc/).
671
672 **Quenching assay**
673 Yeast cells immobilized on concanavalin A-coated glass-bottom dishes (Mattek) were
674 imaged. They were then treated with 500 μL of 1M sodium dithionite dissolved in SDCA
675 medium while being imaged under a microscope.
676
677 **SDS–PAGE and western blotting**
678 Cells cultured in SDCA medium (2 × 10^7 cells per mL) were subjected to lysis using
679 alkaline trichloroacetic acid, followed by SDS–PAGE and western blotting[84]. To analyze
680 Ape1 maturation, expression of Atg2, and GFP–Atg8 processing, SDS–PAGE was
681 performed using 10% acrylamide gels. Proteins were transferred to polyvinylidene
682 fluoride membranes (Immobilon-P; Millipore) using a semi-dry transfer apparatus
683 (Trans-Blot Turbo Transfer System; Bio-Rad) at 2.5 A and 25 V for 15 min. Following
684 the transfer, the membranes were incubated with 2% skim milk in Tris-buffered saline
685 containing 0.05% Tween 20 (TBST) for 30 min at room temperature to block
686 nonspecific binding. The membranes were incubated with primary anti-Ape1
687 (1:10,000), anti-Atg 2 (1:5000), and anti-GFP (1:5000) antibodies for 60 min at room
688 temperature. The membranes were washed thrice with TBST and treated with
689 horseradish peroxidase-labeled anti-rabbit secondary antibody (Promega) at a dilution
690 of 1:5000 for 30 min, followed by an additional wash in TBST. Chemiluminescent
691 signals were generated using an enhanced chemiluminescence reagent (GE
692 Healthcare) and ImmunoStar LD (Fujifilm) then detected using an IR-LAS 1000
693 imaging system (Fujifilm).
694
695 **FRAP measurements and analysis**
696 For the FRAP experiments assessing the IM, cells treated with rapamycin or SDCA-N
697 were seeded onto concanavalin A-coated glass-bottom dishes (Mattek) that
698 immobilized the cells. The experiments were performed using a confocal laser
699 scanning microscope FV-3000 (Olympus) equipped with a UPLSAPO60XO oil-
700 immersion objective lens (1.42 NA; Olympus). For mNG and R18 fluorescence imaging,
701 excitation was performed using a 488 nm laser, and fluorescence was recorded at 561
702 nm in a linear sequential mode. Photobleaching was performed using 488 and 561 nm
703 laser pulses. The images were analyzed using FIJI v.1.52e31. For the kinetic analysis,

the relative fluorescence intensity was plotted against time, with the intensity before quenching set to 1.0 and the minimum intensity after quenching to 0.0. The data were then fitted to an exponential recovery curve: $F = A_0(1 - exp(k_{off}t))$, where t represents time in seconds, and A_0 is the maximum recovery at t = infinity.

Repletion assay using nutrient-rich medium

The cells were grown to the mid-log phase and then shifted to SDCA-N medium (0.17% Difco™ yeast nitrogen base w/o amino acids and ammonium sulfate, 0.5% Bacto™ casamino acids, and 2% glucose) to induce autophagy. The cells were then seeded on concanavalin A-coated glass-bottom dishes (Mattek) to immobilize them and were imaged. Prior to photobleaching, 1 mL of SDCA was added to the glass-bottom dish to terminate autophagy. Photobleaching and time-lapse imaging were then performed.

Molecular modeling using AlphaFold3

Structural prediction of 4 molecules of R18, 12 molecules of DOPE and 12 molecules of POPC bound to Atg2 (residues 1–1346) was performed using AlphaFold3 v3.0.0 installed on a local computer[81]. Structural figures were prepared using PyMOL (http://www.pymol.org/pymol)[85]. A script file to run AlphaFold3 (run_1-1346_12popc_12dope_4r18.sh) and an input JSON file (1-1346_12POPC_12DOPE_4R18.json) are provided as Supplemental Materials.

Statistical analysis

The length of the isolation membrane (IM) was quantified using the segmented line tool in ImageJ, by tracing the contour from one edge of the IM to the opposite edge. The statistical analyses of all experiments were performed using GraphPad Prism software (version 9.5.1).

Summary of Supplemental Materials

Figures S1-S5

Supplemental Video 1-5

Supplemental text 1-2

Acknowledgments

We thank Drs. Christopher. T. Beh, Hitoshi Nakatogawa, Jasper Rine, Ryouichi Fukuda, Kishimoto Takuma, and Kazuma Tanaka for providing plasmids and strains; Dr. Kyoka Sasaki for technical support; Dr. Yoshikazu Ohya for critical advice. We thank Dr. Kazuaki Matoba for performing the lipid transfer assay of the Atg2^{LT} protein. We thank Dr. Masahiko Watanabe for GFP-antibody and Ayaka Saito for assistance with EM sample preparation. We thank the Open Facility, Global Research Facility Alliance Center, Office for Integrated Technical Core Hub, Hokkaido University for allowing us to conduct the analysis of Replica using JEM-1400plus TEM.

This work was supported in part by JSPS KAKENHI Grant Numbers JP19H05707,

JP23K20044, JP23K06667, JP24H00060 (to N.N.N.), JP 20H05313, JP22H02569 (to K.S.), and CREST, Japan Science and Technology Agency Grant number JPMJCR20E3 (to K.S., N.N.N.).

Author contributions

K.S. supervised the project. L.H. and K.S. conceptualized the study and designed the experiments. L.H. performed the experiments and data analysis. T.M. initially visualized the colocalization of R18 and ARSs in yeast cells, and L.H. reproduced and validated these findings. Y.O., Y.H., and N.N.N. imaged the R18 distribution in mammalian cells. T.T. performed the freeze-fracture replica double labeling. T.K constructed the super tether∆ mutant. H.L. provided insights into R18 transport by Osh proteins, and L.H. investigated it. L.H. wrote the original manuscript. L.H. and K.S. revised the manuscript.

Declaration of interests

The authors declare no competition of interests.

References

1. Palade, P. Intracellular Aspects of the Process of Protein Synthesis. *Science* **189**, 347–358 (1975).

2. Acoba, M. G., Senoo, N. & Claypool, S. M. Phospholipid ebb and flow makes mitochondria go. *Journal of Cell Biology* **219**, e202003131 (2020).

3. Wirtz, K. W. A. & Zilversmit, D. B. Exchange of Phospholipids between Liver Mitochondria and Microsomes in Vitro. *Journal of Biological Chemistry* **243**, 3596–3602 (1968).

4. DeGrella, R. F. & Simoni, R. D. Intracellular transport of cholesterol to the plasma membrane. *J Biol Chem* **257**, 14256–14262 (1982).

5. Kaplan, M. R. & Simoni, R. D. Transport of cholesterol from the endoplasmic reticulum to the plasma membrane. *Journal of Cell Biology* **101**, 446–453 (1985).

6. Wirtz, K. W. Phospholipid transfer proteins. *Annu Rev Biochem* **60**, 73–99 (1991).

7. Reinisch, K. M. & Prinz, W. A. Mechanisms of nonvesicular lipid transport. *J Cell Biol* **220**, e202012058 (2021).

8. Prinz, W. A., Toulmay, A. & Balla, T. The functional universe of membrane contact sites. *Nat Rev Mol Cell Biol* **21**, 7–24 (2020).

9. Saheki, Y. & De Camilli, P. Endoplasmic Reticulum-Plasma Membrane Contact Sites. *Annu Rev Biochem* **86**, 659–684 (2017).

10. Wong, L. H., Gatta, A. T. & Levine, T. P. Lipid transfer proteins: the lipid commute via shuttles, bridges and tubes. *Nat Rev Mol Cell Biol* **20**, 85–101 (2019).

11. Sha, B., Phillips, S. E., Bankaitis, V. A. & Luo, M. Crystal structure of the Saccharomyces cerevisiae phosphatidylinositol-transfer protein. *Nature* **391**, 506–510 (1998).

12. Tsujishita, Y. & Hurley, J. H. Structure and lipid transport mechanism of a StAR-related domain. *Nat Struct Biol* **7**, 408–414 (2000).

13. Chiapparino, A., Maeda, K., Turei, D., Saez-Rodriguez, J. & Gavin, A. The orchestra of lipid-transfer proteins at the crossroads between metabolism and signaling. *Prog Lipid Res* **61**, 30–39 (2016).

14. Neuman, S. D., Levine, T. P. & Bashirullah, A. A novel superfamily of bridge-like lipid transfer proteins. *Trends in Cell Biology* **32**, 962–974 (2022).

15. Hanna, M., Guillén-Samander, A. & Camilli, P. D. RBG Motif Bridge-Like Lipid Transport Proteins: Structure, Functions, and Open Questions. *Annual Review of Cell and Developmental Biology* **39**, 409–434 (2023).

16. Maeda, S., Otomo, C. & Otomo, T. The autophagic membrane tether ATG2A transfers lipids between membranes. *Elife* **8**, e45777 (2019).

17. Valverde, D. P. *et al*. ATG2 transports lipids to promote autophagosome biogenesis. *J Cell Biol* **218**, 1787–1798 (2019).

18. Osawa, T. *et al*. Atg2 mediates direct lipid transfer between membranes for autophagosome formation. *Nat Struct Mol Biol* **26**, 281–288 (2019).

19. Toulmay, A. *et al*. Vps13-like proteins provide phosphatidylethanolamine for GPI anchor synthesis in the ER. *Journal of Cell Biology* **221**, e202111095 (2022).

20. Hanna, M. G., Suen, P. H., Wu, Y., Reinisch, K. M. & De Camilli, P. SHIP164 is a chorein motif lipid transfer protein that controls endosome–Golgi membrane traffic. *Journal of Cell Biology* **221**, e202111018 (2022).

21. Guillén-Samander, A. *et al*. VPS13D bridges the ER to mitochondria and peroxisomes via Miro. *Journal of Cell Biology* **220**, e202010004 (2021).

22. Kumar, N. *et al*. VPS13A and VPS13C are lipid transport proteins differentially localized at ER contact sites. *J Cell Biol* **217**, 3625–3639 (2018).

23. Levine, T. P. Sequence Analysis and Structural Predictions of Lipid Transfer Bridges in the Repeating Beta Groove (RBG) Superfamily Reveal Past and Present Domain Variations Affecting Form, Function and Interactions of VPS13, ATG2, SHIP164, Hobbit and Tweek. *Contact (Thousand Oaks)* **5**, 251525642211343 (2022).

24. Braschi, B., Bruford, E. A., Cavanagh, A. T., Neuman, S. D. & Bashirullah, A. The bridge-like lipid transfer protein (BLTP) gene group: introducing new nomenclature based on structural homology indicating shared function. *Human Genomics* **16**, 66 (2022).

25. Maeda, S., Otomo, C. & Otomo, T. The autophagic membrane tether ATG2A transfers lipids between membranes. *elife* **8**, e45777 (2019).

26. Valverde, D. P. *et al*. ATG2 transports lipids to promote autophagosome biogenesis. *J. Cell Biol.* **218**, 1787–1798 (2019).

27. Chowdhury, S. *et al*. Insights into autophagosome biogenesis from structural and biochemical analyses of the ATG2A-WIPI4 complex. *Proceedings of the National Academy of Sciences* **115**, E9792–E9801 (2018).

826 28. Mizushima, N., Yoshimori, T. & Ohsumi, Y. The Role of Atg Proteins in
827 Autophagosome Formation. *Annu. Rev. Cell Dev. Biol.* **27**, 107–132 (2011).

828 29. Suzuki. The pre-autophagosomal structure organized by concerted functions of
829 APG genes is essential for autophagosome formation | The EMBO Journal.

830 30. Kim, J., Huang, W., Stromhaug, P. E. & Klionsky, D. J. Convergence of Multiple
831 Autophagy and Cytoplasm to Vacuole Targeting Components to a Perivacuolar
832 Membrane Compartment Prior tode Novo Vesicle Formation*. *J. Biol. Chem.* **277**,
833 763–773 (2002).

834 31. Wang, Z. & Zhang, H. Phase Separation, Transition, and Autophagic Degradation
835 of Proteins in Development and Pathogenesis. *Trends Cell Biol.* **29**, 417–427 (2019).

836 32. Polyansky, A. *et al*. Phospholipid imbalance impairs autophagosome completion.
837 *EMBO J* **41**, e110771 (2022).

838 33. Schütter, M., Giavalisco, P., Brodesser, S. & Graef, M. Local Fatty Acid
839 Channeling into Phospholipid Synthesis Drives Phagophore Expansion during
840 Autophagy. *Cell* **180**, 135–149.e14 (2020).

841 34. Orii, M., Tsuji, T., Ogasawara, Y. & Fujimoto, T. Transmembrane phospholipid
842 translocation mediated by Atg9 is involved in autophagosome formation. *Journal of*
843 *Cell Biology* **220**, e202009194 (2021).

844 35. Reggiori, F., Tucker, K. A., Stromhaug, P. E. & Klionsky, D. J. The Atg1-Atg13
845 complex regulates Atg9 and Atg23 retrieval transport from the pre-autophagosomal
846 structure. *Developmental cell* **6**, 79–90 (2004).

847 36. Obara, K., Noda, T., Niimi, K. & Ohsumi, Y. Transport of phosphatidylinositol 3-
848 phosphate into the vacuole via autophagic membranes in Saccharomyces cerevisiae.
849 *Genes to Cells* **13**, 537–547 (2008).

850 37. Gómez-Sánchez, R. *et al*. Atg9 establishes Atg2-dependent contact sites
851 between the endoplasmic reticulum and phagophores. *J. Cell Biol.* **217**, 2743–2763
852 (2018).

853 38. Suzuki, K., Kubota, Y., Sekito, T. & Ohsumi, Y. Hierarchy of Atg proteins in pre-
854 autophagosomal structure organization. *Genes to Cells* **12**, 209–218 (2007).

855 39. Shatz, O. *et al*. Rim aperture of yeast autophagic membranes balances cargo
856 inclusion with vesicle maturation. *Dev Cell* **59**, 911–923.e4 (2024).

857 40. Suzuki, K., Akioka, M., Kondo-Kakuta, C., Yamamoto, H. & Ohsumi, Y. Fine
858 mapping of autophagy-related proteins during autophagosome formation in
859 Saccharomyces cerevisiae. *J. Cell. Sci.* **126**, 2534–2544 (2013).

860 41. Graef, M., Friedman, J. R., Graham, C., Babu, M. & Nunnari, J. ER exit sites are
861 physical and functional core autophagosome biogenesis components. *Mol. Biol. Cell*
862 **24**, 2918–2931 (2013).

863 42. Osawa, T. *et al*. Atg2 mediates direct lipid transfer between membranes for
864 autophagosome formation. *Nature Structural & Molecular Biology* **26**, 281–288
865 (2019).

866 43. Hailey, D. W. *et al*. Mitochondria supply membranes for autophagosome
867 biogenesis during starvation. *Cell* **141**, 656–667 (2010).

868 44. Axe, E. L. *et al*. Autophagosome formation from membrane compartments
869 enriched in phosphatidylinositol 3-phosphate and dynamically connected to the
870 endoplasmic reticulum. *J. Cell Biol.* **182**, 685–701 (2008).

871 45. Puri, C. *et al*. The RAB11A-positive compartment is a primary platform for
872 autophagosome assembly mediated by WIPI2 recognition of PI3P-RAB11A.
873 *Developmental cell* **45**, 114–131. e8 (2018).

874 46. Ge, L. *et al*. Remodeling of ER-exit sites initiates a membrane supply pathway for
875 autophagosome biogenesis. *EMBO Rep.* **18**, 1586–1603 (2017).

876 47. van Vliet, A. R. *et al*. ATG9A and ATG2A form a heteromeric complex essential
877 for autophagosome formation. *Mol. Cell* **82**, 4324–4339. e8 (2022).

878 48. Maeda, S. *et al*. Structure, lipid scrambling activity and role in autophagosome
879 formation of ATG9A. *Nature structural & molecular biology* **27**, 1194–1201 (2020).

880 49. Hoekstra, D., Klappe, K., Hoff, H. & Nir, S. Mechanism of Fusion of Sendai Virus:
881 Role of Hydrophobic Interactions and Mobility Constraints of Viral Membrane
882 Proteins: Effects of Polyethylene Glycol. *Journal of Biological Chemistry* **264**, 6786–
883 6792 (1989).

884 50. Hoekstra, D., De Boer, T., Klappe, K. & Wilschut, J. Fluorescence method for
885 measuring the kinetics of fusion between biological membranes. *Biochemistry (N.*
886 *Y.)* **23**, 5675–5681 (1984).

887 51. Hirata, E., Ohya, Y. & Suzuki, K. Atg4 plays an important role in efficient
888 expansion of autophagic isolation membranes by cleaving lipidated Atg8 in
889 Saccharomyces cerevisiae. *PLoS One* **12**, e0181047 (2017).

890 52. Baba, M., Takeshige, K., Baba, N. & Ohsumi, Y. Ultrastructural analysis of the
891 autophagic process in yeast: detection of autophagosomes and their
892 characterization. *J. Cell Biol.* **124**, 903–913 (1994).

893 53. Hirata, E. *et al*. Atg15 in Saccharomyces cerevisiae consists of two functionally
894 distinct domains. *Mol. Biol. Cell* **32**, 645–663 (2021).

895 54. Teter, S. A. *et al*. Degradation of lipid vesicles in the yeast vacuole requires
896 function of Cvt17, a putative lipase. *J. Biol. Chem.* **276**, 2083–2087 (2001).

897 55. Epple, U. D., Eskelinen, E. & Thumm, M. Intravacuolar membrane lysis in
898 Saccharomyces cerevisiae: Does vacuolar targeting of Cvt17/Aut5p affect its
899 function? *J. Biol. Chem.* **278**, 7810–7821 (2003).

900 56. Bernales, S., Schuck, S. & Walter, P. ER-phagy: selective autophagy of the
901 endoplasmic reticulum. *Autophagy* **3**, 285–287 (2007).

902 57. Hamasaki, M., Noda, T., Baba, M. & Ohsumi, Y. Starvation triggers the delivery
903 of the endoplasmic reticulum to the vacuole via autophagy in yeast. *Traffic* **6**, 56–65
904 (2005).

905 58. Mochida, K. *et al*. Receptor-mediated selective autophagy degrades the
906 endoplasmic reticulum and the nucleus. *Nature* **522**, 359–362 (2015).

907 59. Tsuji, T., Hasegawa, J., Sasaki, T. & Fujimoto, T. Definition of
908 phosphatidylinositol 4,5-bisphosphate distribution by freeze-fracture replica labeling.
909 *J Cell Biol* **224**, e202311067 (2024).

910 60. Vida, T. A. & Emr, S. D. A new vital stain for visualizing vacuolar membrane
911 dynamics and endocytosis in yeast. *J. Cell Biol.* **128**, 779–792 (1995).

912 61. Zhu, L., Jorgensen, J. R., Li, M., Chuang, Y. & Emr, S. D. ESCRTs function
913 directly on the lysosome membrane to downregulate ubiquitinated lysosomal
914 membrane proteins. *Elife* **6**, e26403 (2017).

915 62. Seigneuret, M. & Devaux, P. F. ATP-dependent asymmetric distribution of spin-
916 labeled phospholipids in the erythrocyte membrane: relation to shape changes.
917 *Proceedings of the National Academy of Sciences* **81**, 3751–3755 (1984).

918 63. Saito, K. *et al*. Cdc50p, a protein required for polarized growth, associates with
919 the Drs2p P-type ATPase implicated in phospholipid translocation in Saccharomyces
920 cerevisiae. *Mol. Biol. Cell* **15**, 3418–3432 (2004).

921 64. Tanaka, K., Fujimura-Kamada, K. & Yamamoto, T. Functions of phospholipid
922 flippases. *The journal of biochemistry* **149**, 131–143 (2011).

923 65. Hua, Z., Fatheddin, P. & Graham, T. R. An essential subfamily of Drs2p-related
924 P-type ATPases is required for protein trafficking between Golgi complex and
925 endosomal/vacuolar system. *Mol. Biol. Cell* **13**, 3162–3177 (2002).

926 66. Furuta, N., Fujimura-Kamada, K., Saito, K., Yamamoto, T. & Tanaka, K.
927 Endocytic recycling in yeast is regulated by putative phospholipid translocases and
928 the Ypt31p/32p–Rcy1p pathway. *Mol. Biol. Cell* **18**, 295–312 (2007).

929 67. Jain, B. K. *et al*. P4-ATPases control phosphoinositide membrane asymmetry
930 and neomycin resistance. *Nat Cell Biol* **27**, 1114–1124 (2025).

931 68. Hao, L., Zhao, C. & Suzuki, K. Monitoring phospholipid dynamics in vivo with a
932 fluorescent dye octadecyl rhodamine B. *Cell Struct Funct* (2025).

933 69. Manford, A. G., Stefan, C. J., Yuan, H. L., Macgurn, J. A. & Emr, S. D. ER-to-
934 plasma membrane tethering proteins regulate cell signaling and ER morphology. *Dev*
935 *Cell* **23**, 1129–1140 (2012).

936 70. Lev, S. Non-vesicular lipid transport by lipid-transfer proteins and beyond. *Nature*
937 *reviews Molecular cell biology* **11**, 739–750 (2010).

938 71. Stefan, C. J. *et al*. Osh proteins regulate phosphoinositide metabolism at ER-
939 plasma membrane contact sites. *Cell* **144**, 389–401 (2011).

940 72. Kentala, H., Weber-Boyvat, M. & Olkkonen, V. M. in *International Review of Cell*
941 *and Molecular Biology* (ed Jeon, K. W.) 299–340 (Academic Press, 2016).

942 73. Albulescu, L. *et al*. Broad-range inhibition of enterovirus replication by OSW-1, a
943 natural compound targeting OSBP. *Antiviral Res* **117**, 110–114 (2015).

944 74. Burgett, A. W. G. *et al*. Natural products reveal cancer cell dependence on
945 oxysterol-binding proteins. *Nat Chem Biol* **7**, 639–647 (2011).

946 75. Srinivasan, S., Álvarez, D., John Peter, A. T. & Vanni, S. Unbiased MD
947 simulations identify lipid binding sites in lipid transfer proteins. *J. Cell Biol.* **223**,
948 e202312055 (2024).

949 76. Dabrowski, R., Tulli, S. & Graef, M. Parallel phospholipid transfer by Vps13 and
950 Atg2 determines autophagosome biogenesis dynamics. *J Cell Biol* **222**, e202211039
951 (2023).

952 77. Sakai, Y. *et al*. Mechanism of bridge-type phospholipid transfer by Atg2 for
953 autophagosome biogenesis. , 2025.05.24.655882 (2025).

954 78. Stachowiak, J. C. & Kirchhausen, T. The beauty of simplicity in membrane
955 biology. *Nat. Cell Biol.*, 1–4 (2022).

956 79. Takar, M., Wu, Y. & Graham, T. R. The essential Neo1 protein from budding
957 yeast plays a role in establishing aminophospholipid asymmetry of the plasma
958 membrane. *J. Biol. Chem.* **291**, 15727–15739 (2016).

959 80. Nakatogawa, H., Suzuki, K., Kamada, Y. & Ohsumi, Y. Dynamics and diversity in
960 autophagy mechanisms: lessons from yeast. *Nature reviews Molecular cell biology*
961 **10**, 458–467 (2009).

962 81. Abramson, J. *et al*. Accurate structure prediction of biomolecular interactions with
963 AlphaFold 3. *Nature* **630**, 493–500 (2024).

964 82. Gietz, R. D. & Woods, R. A. Transformation of yeast by lithium acetate/single-
965 stranded carrier DNA/polyethylene glycol method. *Methods Enzymol* **350**, 87–96
966 (2002).

967 83. Kaiser, C., Michaelis, S. & Mitchell, A. in *Methods in yeast genetics* (Cold Spring
968 Harbor Laboratory Press Cold Spring Harbor, NY, 1994).

969 84. Horvath, A. & Riezman, H. Rapid protein extraction from Saccharomyces
970 cerevisiae. *Yeast* **10**, 1305–1310 (1994).

971 85. The PyMOL Molecular Graphics System, Version 2.0 Schrödinger, LLC.

972

Figures

Figure 1

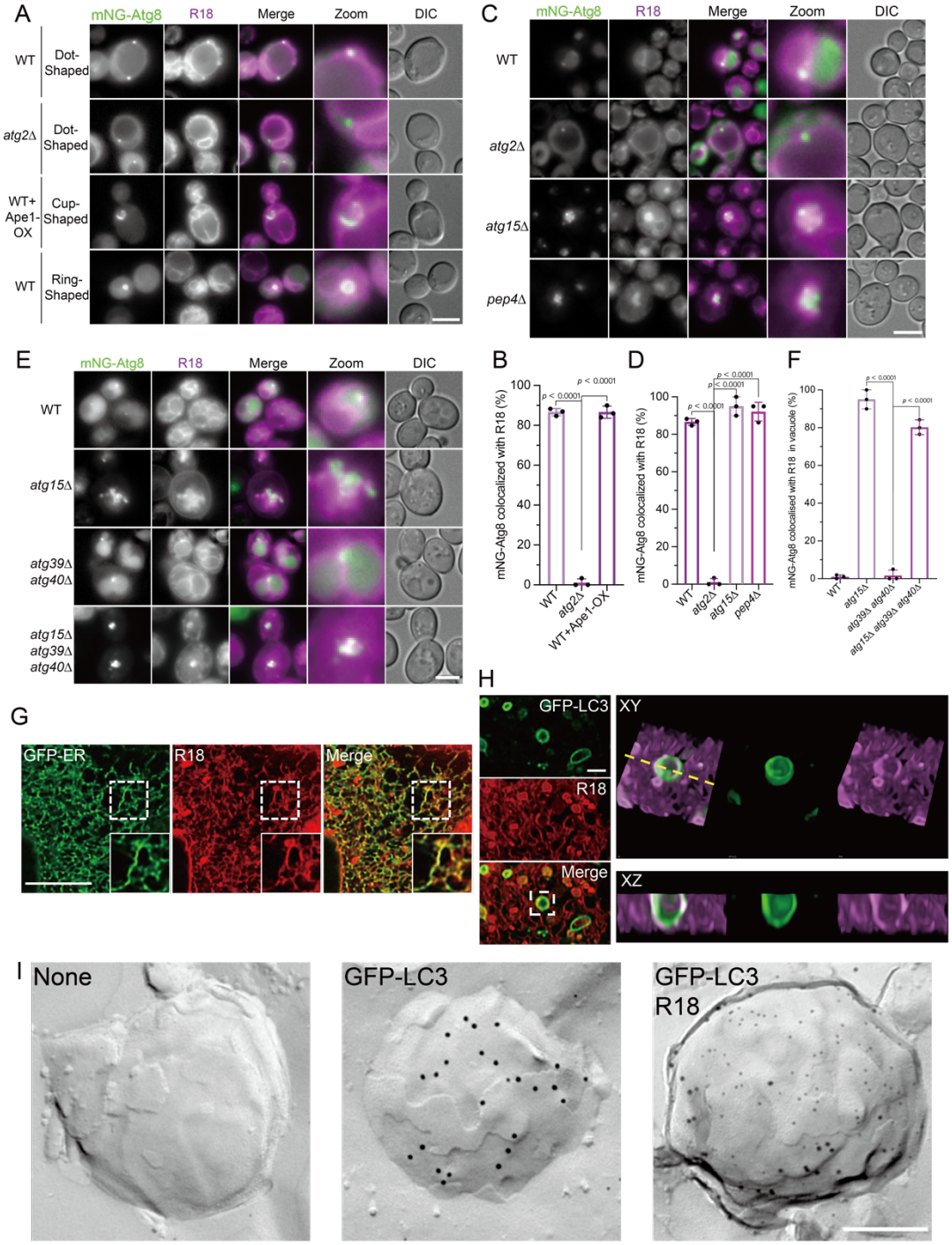

973

Figure 1 Octadecyl rhodamine B (R18) stains autophagy-related membrane structures.

(A) Colocalization between mNG–Atg8 and R18 in W303 background cells treated with rapamycin to induce autophagy. Cells were stained with R18 for 10 minutes, washed with fresh medium, and then treated with 200 ng/mL rapamycin for 1 hour before imaging. The scale bar represents 5 μm. WT, wild-type. OX, overexpression. mNG, mNeonGreen. DIC, differential interference contrast.

(B) Percentage of colocalization calculated using 100 cells from 3 independent experiments in (A). WT includes both dot- and ring-like structures of mNG–Atg8 colocalized with R18. Error bars represent standard deviation (SD). P-values were calculated using one-way ANOVA.

(C) Colocalization between mNG–Atg8 and R18 in SEY6210 background cells. Cells were stained with R18 for 10 minutes, washed with fresh medium, and then treated with 200 ng/mL rapamycin for 1 hour before imaging. The scale bar represents 5 μm.

(D) Percentage of colocalization calculated using 100 cells from 3 independent experiments in (C). Error bars represent SD. P-values were calculated using one-way ANOVA.

(E) Colocalization between mNG–Atg8 and R18 in SEY6210 background cells. Cells were stained with R18 for 10 minutes, washed with fresh medium, and then treated with 200 ng/mL rapamycin for 1 hour before imaging. The scale bar represents 5 μm.

(F) Percentage of colocalization calculated using 100 cells from 3 independent experiments in (E). Error bars represent SD. P-values were calculated using one-way ANOVA.

(G) MEFs expressing GFP–ER were stained with R18 for colocalization analysis. The boxed area represents a higher magnification.

(H) MEFs expressing GFP–LC3 were subjected to autophagy induction by starvation and stained with R18 for colocalization analysis. The boxed area represents a higher magnification.

(I) Freeze-fracture replica double labeling of R18 and GFP–LC3 in MEF cells. Starved MEFs expressing GFP–LC3 were processed for freeze-fracture replica immunogold labeling. R18 was detected using 6-nm colloidal gold, and GFP–LC3 with 12-nm gold. The scale bar represents 200 nm.

Figure 2

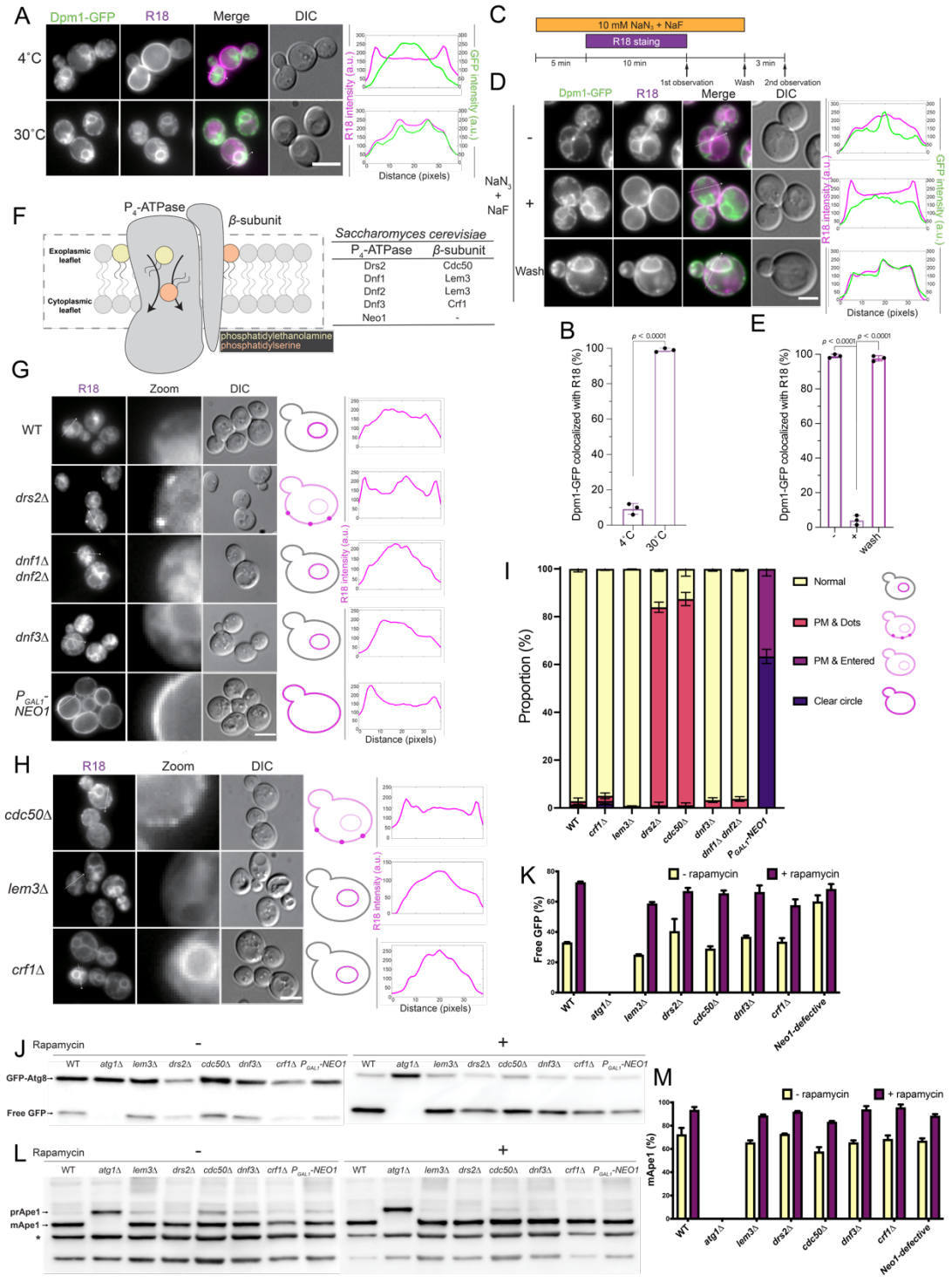
A
Dpm1-GFP
R18
Merge
DIC
4°C
30°C
R18 intensity (a.u.)
GFP intensity (a.u.)
Distance (pixels)
C
10 mM NaN3 + NaF
R18 staing
5 min
10 min
3 min
1st observation
Wash
2nd observation
D
NaN3 + NaF
Wash
F
P4-ATPase
β-subunit
Exoplasmic leaflet
Cytoplasmic leaflet
phosphatidylethanolamine
phosphatidylserine
Saccharomyces cerevisiae
P4-ATPase
β-subunit
Drs2
Cdc50
Dnf1
Lem3
Dnf2
Lem3
Dnf3
Crf1
Neo1
-
B
Dpm1-GFP colocalized with R18 (%)
p < 0.0001
4°C
30°C
E
wash
G
R18
Zoom
DIC
WT
drs2Δ
dnf1Δ dnf2Δ
dnf3Δ
PGAL1-NEO1
H
cdc50Δ
lem3Δ
crf1Δ
I
Proportion (%)
Normal
PM & Dots
PM & Entered
Clear circle
WT
crf1Δ
lem3Δ
drs2Δ
cdc50Δ
dnf3Δ
dnf1Δ dnf2Δ
PGAL1-NEO1
K
- rapamycin
+ rapamycin
Free GFP (%)
atg1Δ
Neo1-defective
J
Rapamycin
GFP-Atg8
Free GFP
L
prApe1
mApe1
M
mApe1 (%)

Figure 2 R18 internalization at the plasma membrane requires flippase activity.
(A) Colocalization between Dpm1–GFP and R18 in WT cells. The cells were stained with R18 at the indicated temperature. The scale bar represents 5 μm. Graphs represent the line profiles of the fluorescence intensity from the images on the left.
(B) Percentage of colocalization calculated using 100 cells from 3 independent experiments in (A). Error bars represent SD. P-values were calculated using an unpaired student's t-test.
(C) Illustration of the imaging process in (D). Cells were treated with NaN_3 and NaF for 5 min and then with R18 for 10 min while incubating with ATP inhibitors for the first observation. After removing NaN_3 and NaF after a 3-min wash, the cells were observed again.
(D) Colocalization between Dpm1–GFP and R18 in WT cells treated with/without NaN_3 and NaF, followed by washing out the inhibitors. The scale bar represents 5 μm. Graphs indicate the line profiles of the fluorescence intensity from the images on the left.
(E) Percentage of colocalization calculated using 100 cells from 3 independent experiments in (D). Error bars represent SD. P-values were calculated using one-way ANOVA.
(F) Model of the P4-ATPase flippase. The ATPase forms a functional complex with the β-subunit to translocate phosphatidylserine (PS) and phosphatidylethanolamine (PE) from the exoplasmic to the cytoplasmic leaflet. There are five types of flippases, and their subunits in *S. cerevisiae* are listed.
(G) R18 distribution in flippase-defective cells. *drs2*Δ cells exhibit a dot pattern (marked by arrows in the image), *dnf1*Δ *dnf2*Δ and *dnf3*Δ cells exhibit an ER pattern, and the suppression of Neo1 shows a clear circle pattern. The scale bar represents 5 μm. The phenotypes of the yeast cells representing each pattern are illustrated to the right. Graphs indicate the line profiles of the fluorescence intensity in the images on the left.
(H) R18 distribution in β-subunit deletion cells. *cdc50*Δ cells exhibit a dot pattern (marked by arrows in the image) that phenocopies the pattern observed in *drs2*Δ cells. *lem3*Δ and *crf1*Δ cells exhibit an ER pattern that phenocopies the pattern observed in *dnf1*Δ *dnf2*Δ and *dnf3*Δ cells. The phenotypes of the yeast cells representing each pattern are illustrated to the right. The scale bar represents 5 μm. Graphs indicate the line profiles of the fluorescence intensity in the images on the left.
(I) Graph representing the proportion (average ± SD) of cells with different patterns. n > 100 cells in 3 independent experiments.
(J) Autophagic activity of flippase-defective cells measured using the GFP–Atg8 processing assay. WT and flippase-defective cells carrying a GFP–Atg8 plasmid were treated with 200 ng/mL rapamycin for 2 h to induce autophagy. Western blot analysis was performed using anti-GFP antibodies. The upper bands represent GFP-tagged Atg8 (GFP-Atg8), and the lower bands represent cleaved GFP (free GFP).
(K) Quantification of the free-GFP / GFP–Atg8 ratio (mean ± SD, from three independent experiments).

1050 (L) The same samples are used in (J). Western blot analysis was performed using an
1051 anti-Ape1 antibody. The upper bands represent precursor Ape1 (prApe1), the middle
1052 bands represent mature Ape1 (mApe1), and the lower bands represent nonspecific
1053 signals that can be used as an internal control (*).
1054 (M) Quantification of the mApe1/total Ape1 ratio (mean ± SD, from three independent
1055 experiments).

Figure 3

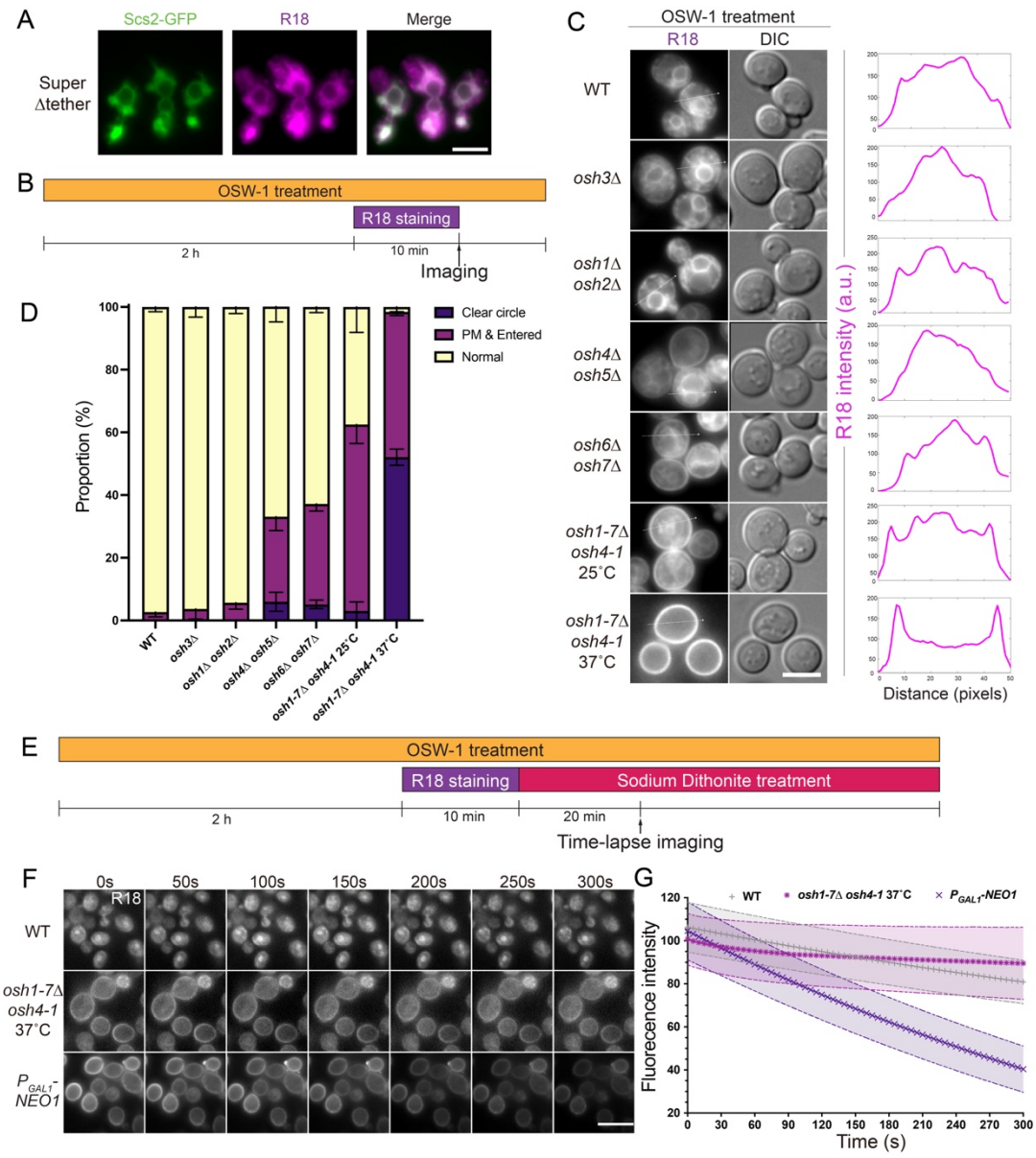
A
Scs2-GFP
R18
Merge
Super Δtether
B
OSW-1 treatment
R18 staining
2 h
10 min
Imaging
C
OSW-1 treatment
R18
DIC
WT
osh3Δ
osh1Δ osh2Δ
osh4Δ osh5Δ
osh6Δ osh7Δ
osh1-7Δ osh4-1 25˚C
osh1-7Δ osh4-1 37˚C
R18 intensity (a.u.)
Distance (pixels)
D
Proportion (%)
Clear circle
PM & Entered
Normal
WT
osh3Δ
osh1Δ osh2Δ
osh4Δ osh5Δ
osh6Δ osh7Δ
osh1-7Δ osh4-1 25˚C
osh1-7Δ osh4-1 37˚C
E
OSW-1 treatment
R18 staining
Sodium Dithonite treatment
2 h
10 min
20 min
Time-lapse imaging
F
0s
50s
100s
150s
200s
250s
300s
R18
WT
osh1-7Δ osh4-1 37˚C
P GAL1-NEO1
G
WT
osh1-7Δ osh4-1 37˚C
P GAL1-NEO1
Fluorescence intensity
Time (s)

1056 **Figure 3 R18 transfer from the plasma membrane to the ER requires oxysterol-**
1057 **binding protein (OSBP)-related proteins (ORPs).**
1058 (A) Colocalization between Scs2–GFP and R18 in super tetherΔ cells. The scale bar
1059 represents 5 μm.
1060 (B) The procedure for the experiment in (C). Cells were stained with R18 in the
1061 presence of 10 μM OSW-1.
1062 (C) R18 distribution in WT and Osh deletion cells. Graphs indicate the line profiles of
1063 the fluorescence intensity in the images on the left. The scale bar represents 5 μm.
1064 (D) Graph representing the proportion (average ± SD) of cells with different patterns.
1065 n > 100 cells in 3 independent experiments.
1066 (E) The procedure for the experiment in (F). Cells were stained with R18 in the
1067 presence of 10 μM OSW-1. Imaging was started 20 min after the sodium dithionite
1068 treatment.
1069 (F) Time-lapse imaging of WT, Osh deletion, and Neo1-suppressive cells. The scale
1070 bar represents 10 μm.
1071 (G) Fluorescence intensity of R18 during the time-lapse imaging in (F). Error bars
1072 represent SD; n = 7.

Figure 4

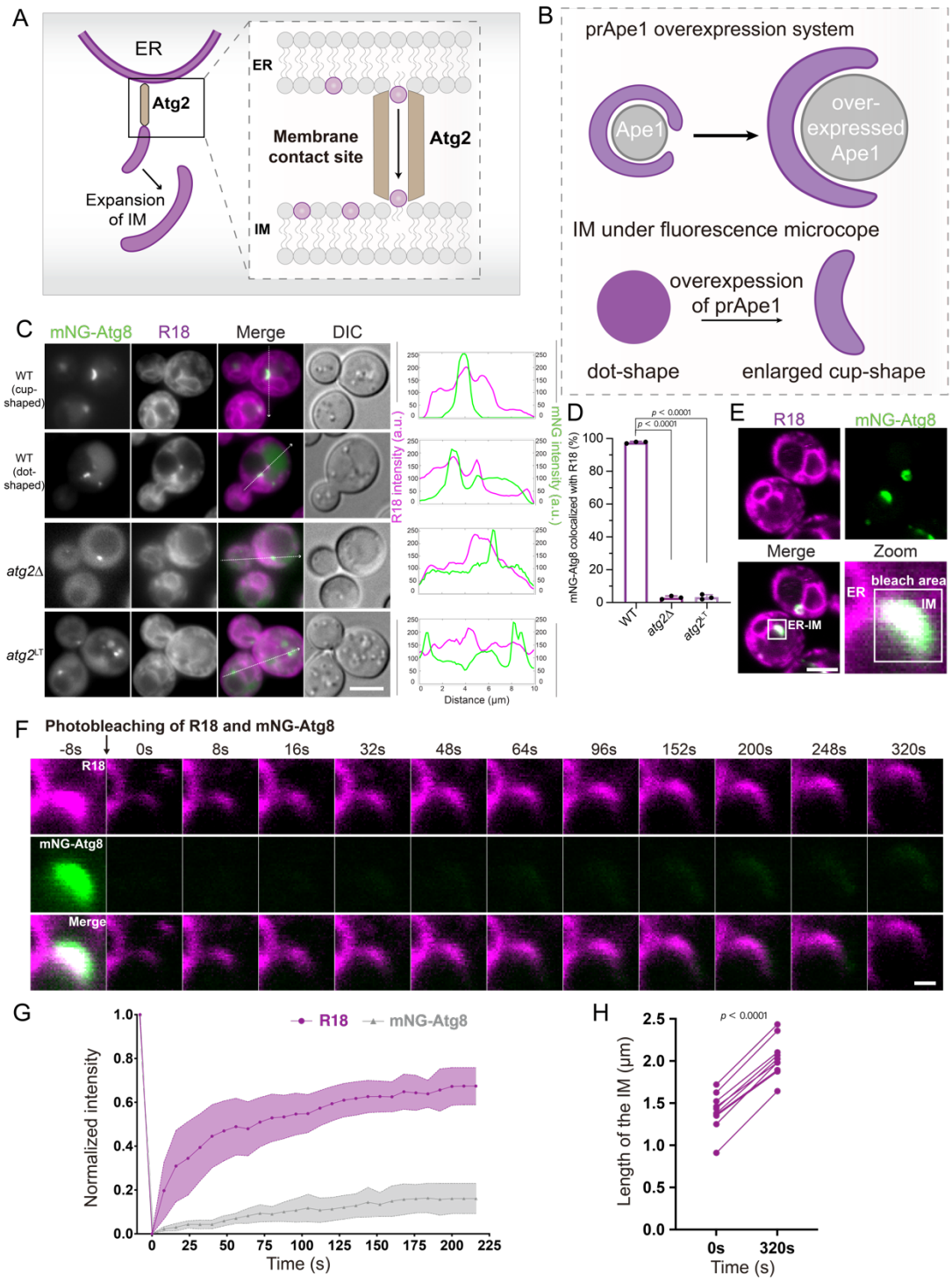
A
ER
Atg2
Expansion of IM
ER
Membrane contact site
Atg2
IM
B
prApe1 overexpression system
Ape1
over-expressed Ape1
IM under fluorescence microcope
overexpression of prApe1
dot-shape
enlarged cup-shape
C
mNG-Atg8
R18
Merge
DIC
WT (cup-shaped)
WT (dot-shaped)
atg2Δ
atg2LT
R18 intensity (a.u.)
mNG intensity (a.u.)
Distance (μm)
D
p < 0.0001
p < 0.0001
mNG-Atg8 colocalized with R18 (%)
WT
atg2Δ
atg2LT
E
R18
mNG-Atg8
Merge
Zoom
ER-IM
ER
bleach area
IM
F
Photobleaching of R18 and mNG-Atg8
-8s
0s
8s
16s
32s
48s
64s
96s
152s
200s
248s
320s
R18
mNG-Atg8
Merge
G
R18
mNG-Atg8
Normalized intensity
Time (s)
H
p < 0.0001
Length of the IM (μm)
0s
320s
Time (s)

1073 **Figure 4 Phospholipids are transferred from the ER to the IM at the ER–IM MCS**
1074 **via Atg2.**
1075 (A) Model of lipid transfer activity from the ER to the IM via Atg2 at the ER–IM MCS.
1076 (B) Visualization of the IM as a cup-shaped structure induced by prApe1
1077 overexpression.
1078 (C) Colocalization between mNG-Atg8 and R18 in WT, *atg2*Δ, and *atg2*^{LT} mutant
1079 cells. The scale bar represents 5 μm. Graphs represent the line profiles of the
1080 fluorescence intensity from the images on the left.
1081 (D) Percentage of colocalization calculated using 100 cells from 3 independent
1082 experiments in (C). WT includes both dot- and cup- shaped colocalization. Error bars
1083 represent SD. P-values were calculated using one-way ANOVA.
1084 (E) IM (mNG–Atg8) is labeled with R18 in prApe1-overexpressing WT cells and
1085 visualized under the confocal microscope. The square indicates the area that was
1086 photobleached. The scale bar represents 5 μm.
1087 (F) FRAP analysis. Images were captured at the indicated time points. The scale bar
1088 represents 1 μm.
1089 (G) Fluorescence recovery of the IM (mNG-Atg8) and R18 after photobleaching.
1090 Error bars represent SD; n = 7.
1091 (H) Quantification of the length of the IM at 0 and 320 s. p-values were calculated
1092 using a two-sided paired student's t-test.

Figure 5

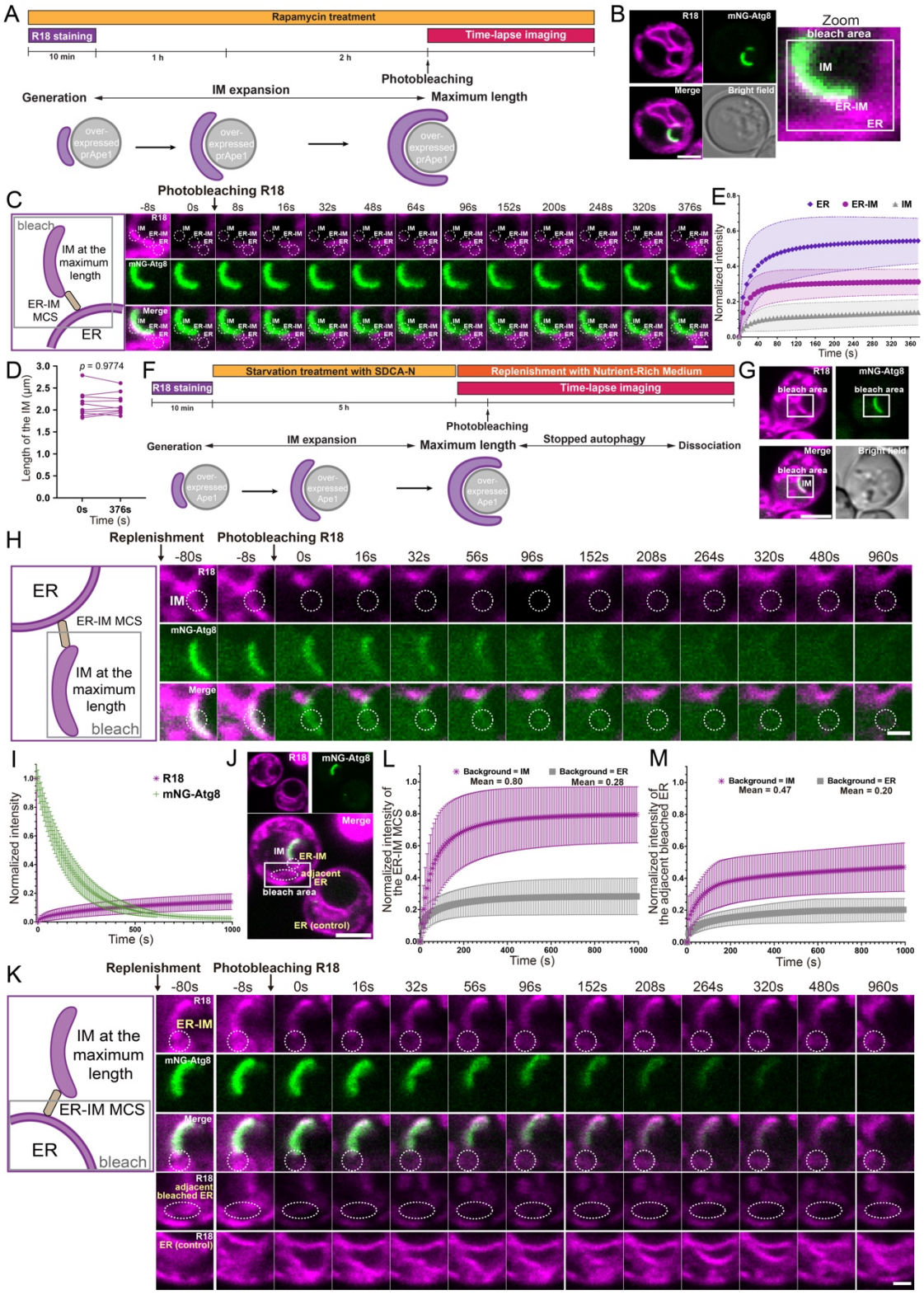
A
Rapamycin treatment
R18 staining
Time-lapse imaging
10 min
1 h
2 h
Photobleaching
Generation
IM expansion
Maximum length
over-expressed prApe1
B
R18
mNG-Atg8
Merge
Bright field
Zoom
bleach area
IM
ER-IM
ER
C
Photobleaching R18
-8s
0s
8s
16s
32s
48s
64s
96s
152s
200s
248s
320s
376s
bleach
IM at the maximum length
ER-IM MCS
ER
E
ER
ER-IM
IM
Normalized intensity
Time (s)
D
p = 0.9774
Length of the IM (μm)
0s
376s
Time (s)
F
Starvation treatment with SDCA-N
Replenishment with Nutrient-Rich Medium
R18 staining
Time-lapse imaging
10 min
5 h
Photobleaching
Generation
IM expansion
Maximum length
Stopped autophagy
Dissociation
over-expressed Ape1
G
R18
mNG-Atg8
bleach area
Merge
Bright field
H
Replenishment
Photobleaching R18
-80s
-8s
0s
16s
32s
56s
96s
152s
208s
264s
320s
480s
960s
ER
ER-IM MCS
IM at the maximum length
bleach
I
R18
mNG-Atg8
Normalized intensity
Time (s)
J
R18
mNG-Atg8
Merge
IM
ER-IM
adjacent ER
bleach area
ER (control)
L
Background = IM
Mean = 0.80
Background = ER
Mean = 0.28
Normalized intensity of the ER-IM MCS
Time (s)
M
Background = IM
Mean = 0.47
Background = ER
Mean = 0.20
Normalized intensity of the adjacent bleached ER
Time (s)
K
Replenishment
Photobleaching R18
-80s
-8s
0s
16s
32s
56s
96s
152s
208s
264s
320s
480s
960s
IM at the maximum length
ER-IM MCS
ER
bleach
R18
ER-IM
mNG-Atg8
Merge
R18 adjacent bleached ER
R18 ER (control)

Figure 5 Phospholipids are transferred from the IM back to the ER after the termination of autophagy.

(A) Procedure for the experiment in (C). prApe1-overexpressed cells were treated with rapamycin, and the FRAP analysis was performed as indicated.

(B) The IM (mNG–Atg8) is labeled with R18 in prApe1-overexpressing WT cells under the confocal microscope. The square indicates the area that is to be photobleached in (C). The scale bar represents 2 μm.

(C) Schematic drawing of the photobleached area (left). During the FRAP analysis, the fluorescence intensity of R18 at three points (ER, ER–IM, and IM) was monitored (right). Images were captured as indicated. The scale bar represents 1 μm.

(D) Quantification of the length of the IM after reaching a maximum length. P-values were calculated using a two-sided paired student's t-test.

(E) Fluorescence recovery of R18 at the IM, ER–IM, and ER after photobleaching. Error bars represent SD; n = 7.

(F) The procedure for the experiments in (H and K). prApe1-overexpressing cells were starved in SDCA-N medium for 5 h, and nutrient-rich medium was then added to terminate autophagy, followed by FRAP analysis as indicated.

(G) IM (mNG–Atg8) is labeled with R18 in prApe1-overexpressing WT cells and visualized under a confocal microscope. The square indicates the area that was photobleached in (H). The scale bar represents 2 μm.

(H) Schematic drawing of the photobleached area (left). The fluorescence intensities of mNG–Atg8 and R18 at the IM were monitored (right). Images were captured as indicated. The scale bar represents 1 μm.

(I) Fluorescence recovery of mNG-Atg8 and R18 at the IM after photobleaching. Error bars represent SD; n = 7.

(J) IM (mNG–Atg8) is labeled with R18 in prApe1-overexpressing WT cells and visualized under a confocal microscope. The square indicates the area that was photobleached in (K). The scale bar represents 5 μm.

(K) Schematic drawing of the photobleached area (left). The fluorescence intensity of R18 at the ER–IM MCS was monitored (right). The scale bar represents 1 μm.

(L) Fluorescence recovery of R18 at the ER–IM MCS, calculated using the IM and unbleached ER as background references. Mean represents the average recovery level at the final timepoint. Error bars represent SD; n = 7.

(M) Fluorescence recovery of R18 at the bleached ER adjacent to the ER–IM MCS, calculated using the IM and unbleached ER as background references. Mean represents the average recovery level at the final timepoint. Error bars represent SD; n = 7.

Figure 6

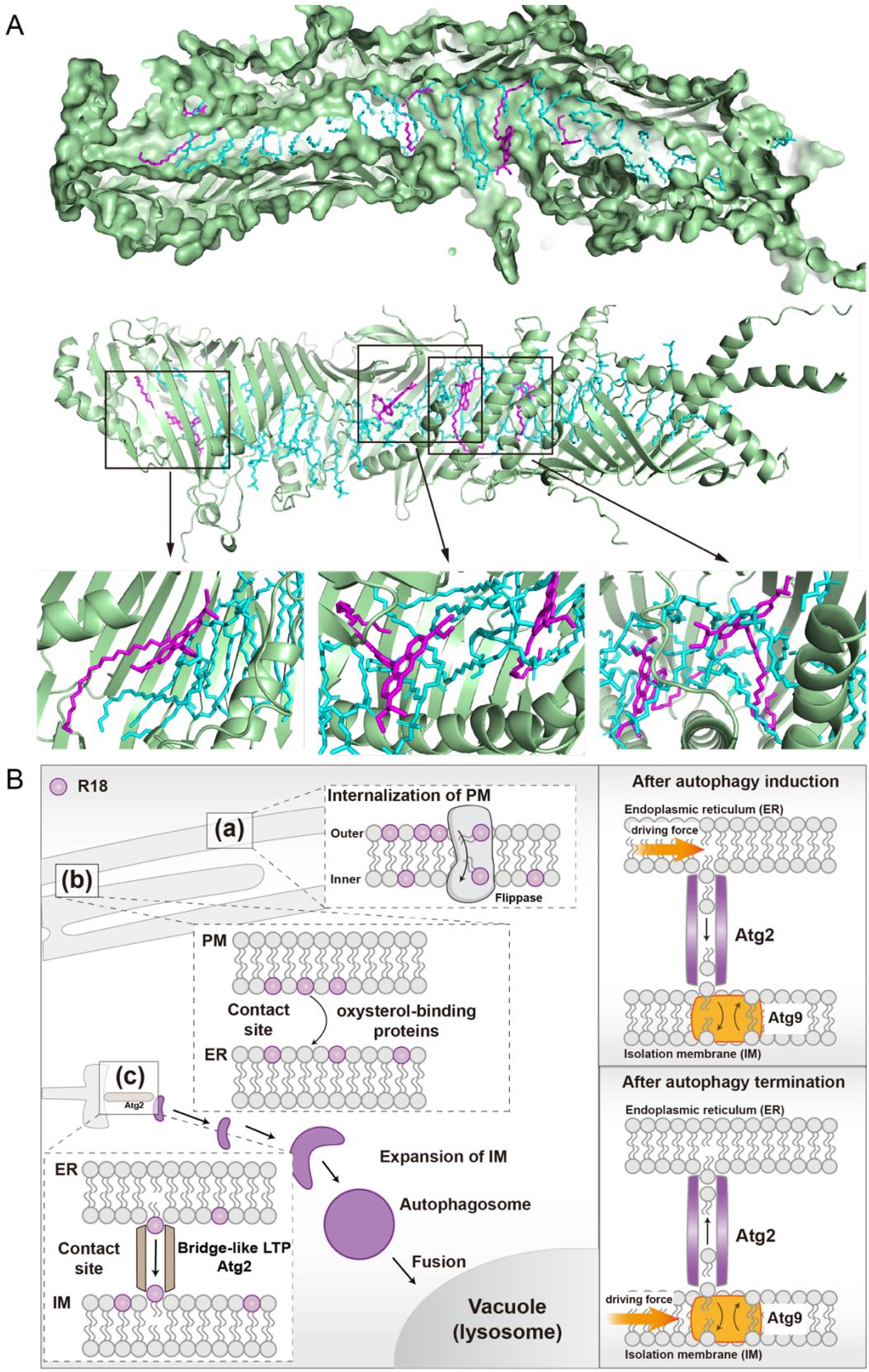

1131

Figure 6 Models for R18 transport from the PM to the IM.

(A) AlphaFold3 model containing Atg2 (1–1346), 12×POPC, 12×DOPE and 4×R18. Cyan represents POPC and DOPE, and magenta represents R18.

(B) Models of the R18 transfer route to the IM (left). Reversible one-way lipid transfer model of Atg2 (right).

1137 **Supplemental Information**

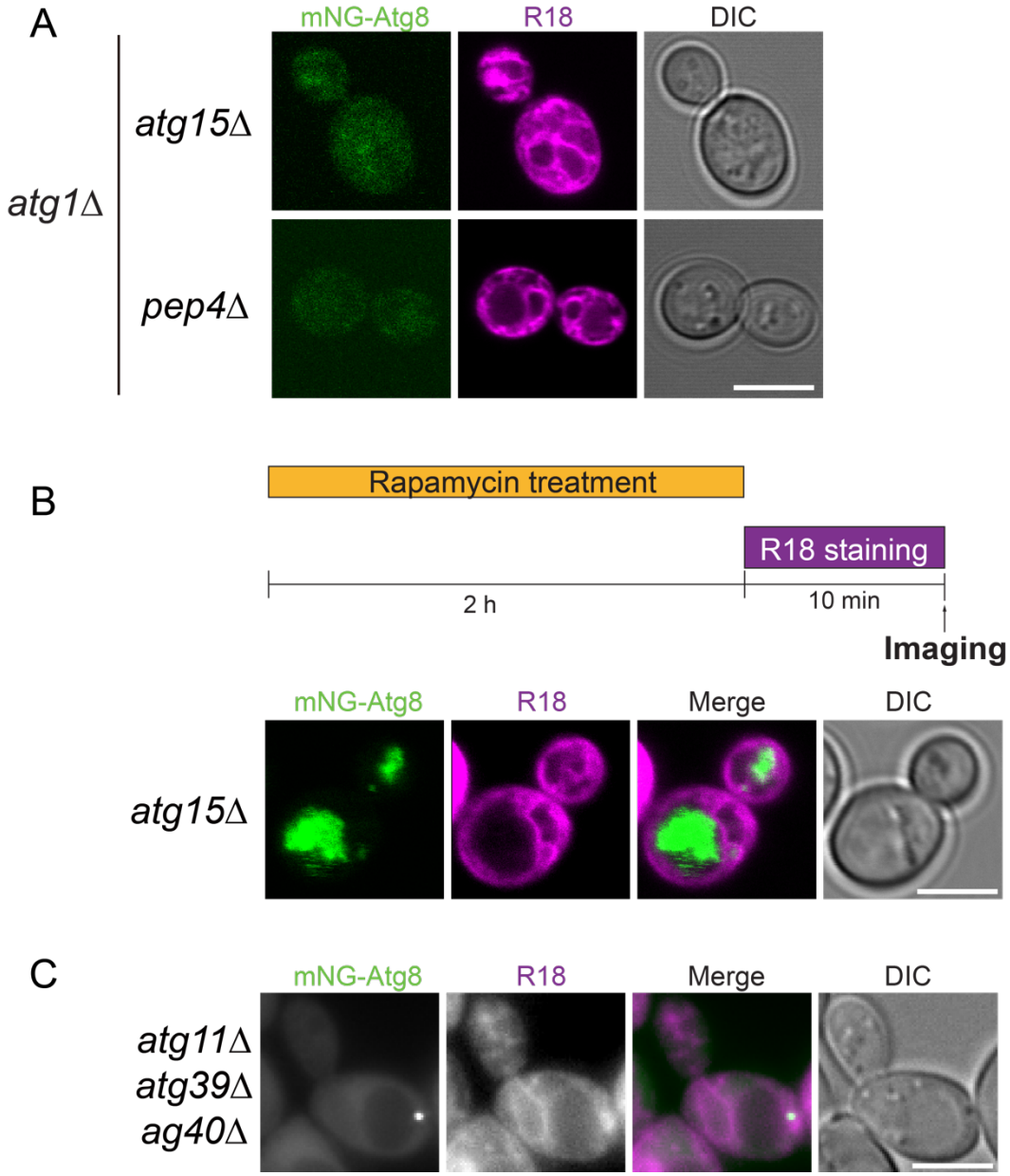

1138

1139

1140 **Figure S1. R18 staining ARSs depends on autophagy**

(A) mNG–Atg8 and R18 staining in *atg1*Δ *atg15*Δ and *atg1*Δ *pep4*Δ cells. Cells were stained with R18 for 10 minutes, washed with fresh medium, and then treated with 200 ng/mL rapamycin for 1 hour before imaging. The scale bar represents 5 μm.

(B) Schematic of rapamycin treatment and R18 staining. Colocalization of mNG–Atg8 and R18 in *atg15*Δ cells following indicated treatment. The scale bar represents 5 μm.

(C) R18 labeling in *atg11*Δ *atg39*Δ *atg40*Δ cells. Cells were stained with R18 for 10 minutes, washed with fresh medium, and then treated with 200 ng/mL rapamycin for 1 hour before imaging. The scale bar represents 5 μm.

1141

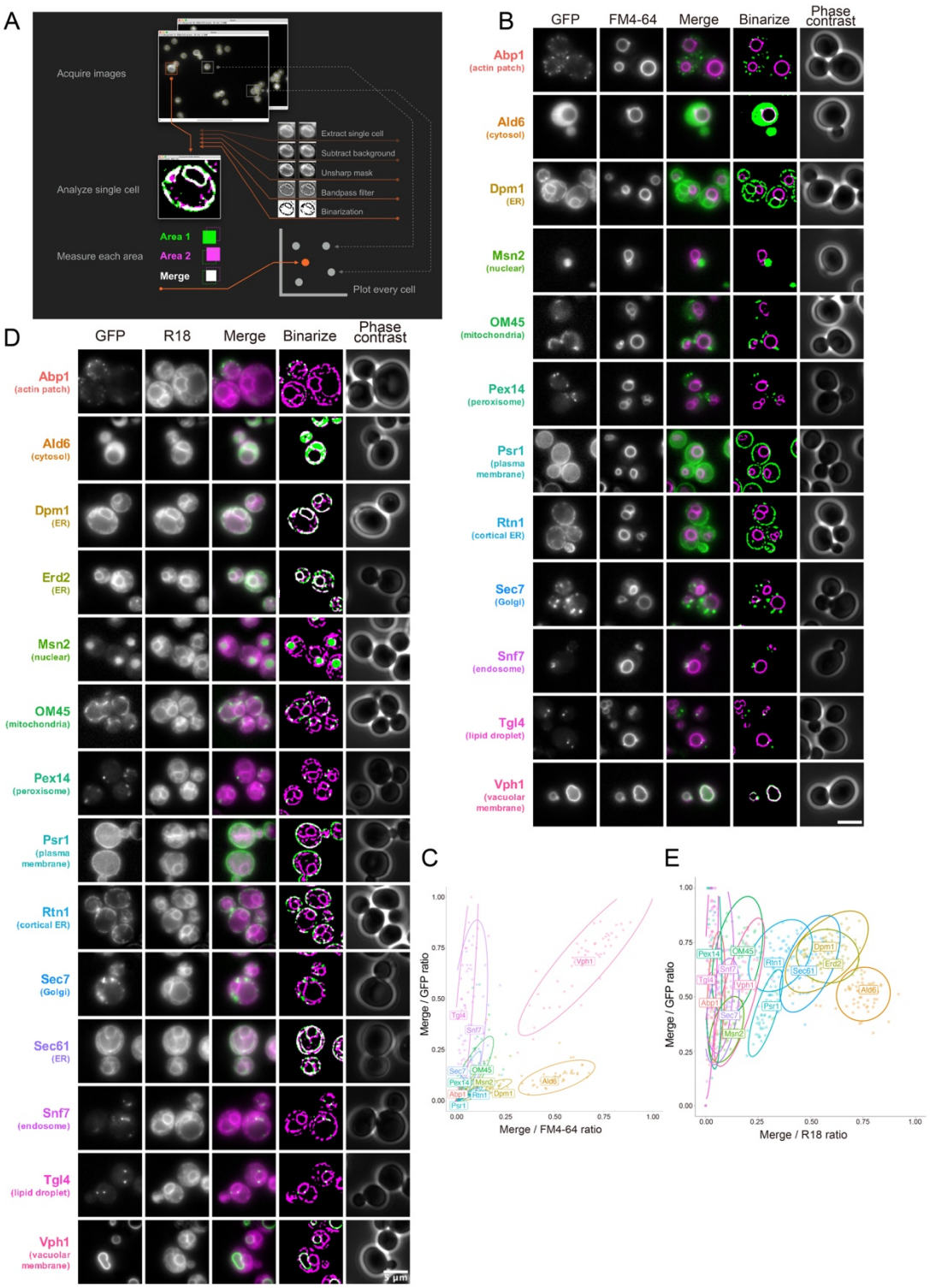

1142 **Figure S2. Localization analysis of FM4-64 and R18**

1143 (A) Single-cell images were extracted from the acquired images. Background
1144 brightness was subtracted using the rolling ball algorithm. Images were sharpened
1145 using unsharp masking and filtered with a bandpass filter to detect drastic intensity
1146 changes. Each structure was extracted through binarization and subsequently

merged. Three areas—each fluorescence-labeled area and merged area—were measured.

(B) Cells expressing GFP-tagged organelle marker proteins were grown in SDCA medium until they reached the mid-log phase and were stained with 8 μM FM4-64. The scale bar represents 5 μm.

(C) Scatter plot of the merge/FM4-64 ratio (x-axis) versus the merge/GFP ratio (y-axis) with a 95% probability ellipse. At least 50 cells were analyzed for each strain.

(D) Cell expressing GFP-labeled organelle marker proteins were grown in SDCA medium until they reached the mid-log phase and were stained with 10 μg/mL of R18.

(E) Scatter plot of the merge/R18 ratio (x-axis) versus the merge/GFP ratio (y-axis) with a 95% probability ellipse. At least 50 cells were analyzed for each strain. The scale bar represents 5 μm.

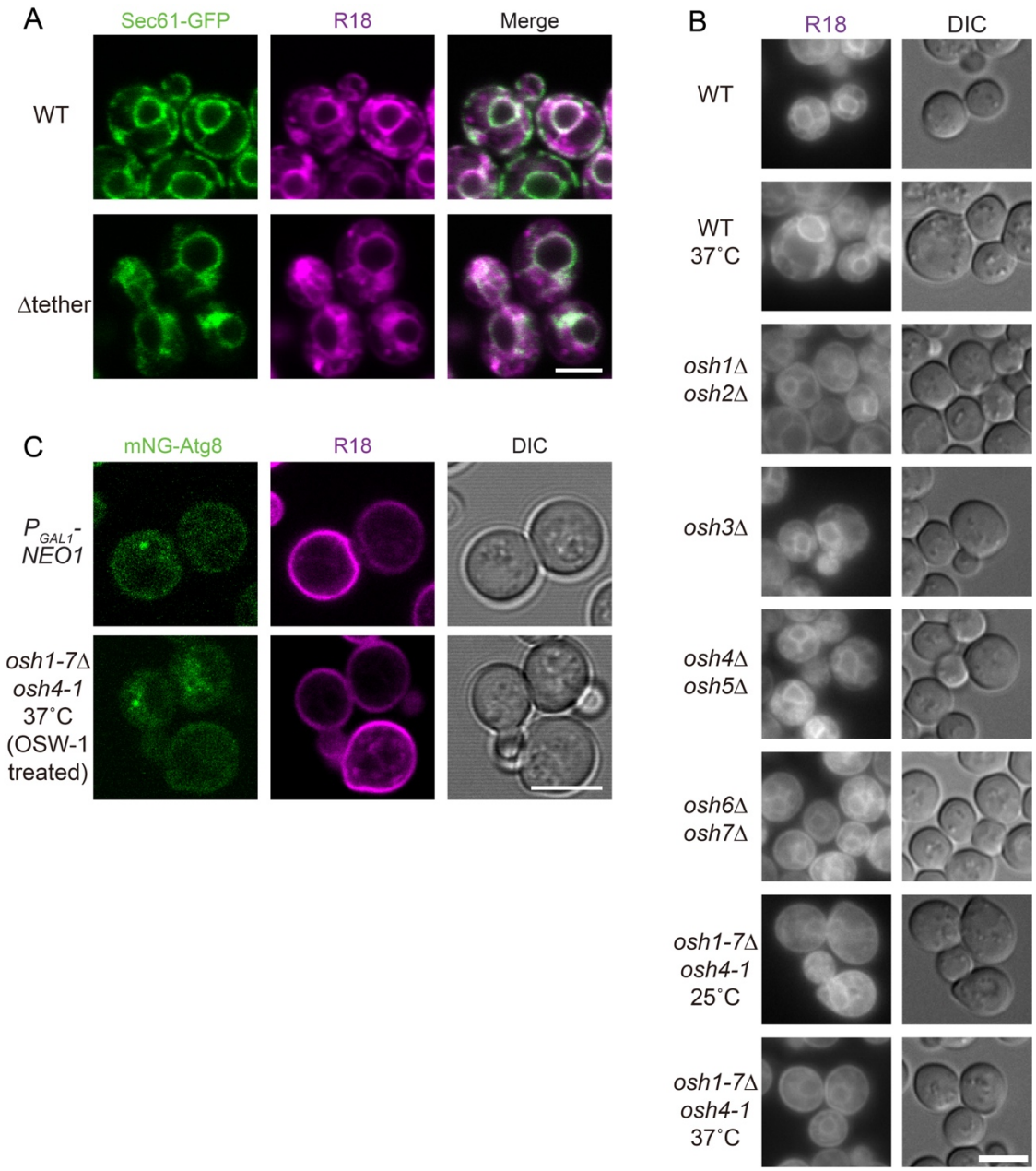

Figure S3. R18 distribution in the Osh and flippase mutants

(A) R18 labeling of the ER in wild-type and tetherΔ cells. The scale bar represents 5 μm.

(B) Cells were grown in SDCA medium to the mid-log phase at 25ºC. Then, cells indicated by "37ºC" were preincubated at 37°C for 1 h. The cells were stained with R18 at the indicated temperature for 10 min and then washed with fresh medium. WT, wild-type. DIC, differential interference contrast. The scale bar represents 5 μm.

(C) R18 staining in flippase- or OSBP-defective cells. NEO1-defective cells and OSBP-defective cells were stained with R18. Cells were stained with R18 for 10 minutes, washed with fresh medium, and then treated with 200 ng/mL rapamycin for 1 hour before imaging. The scale bar represents 5 μm.

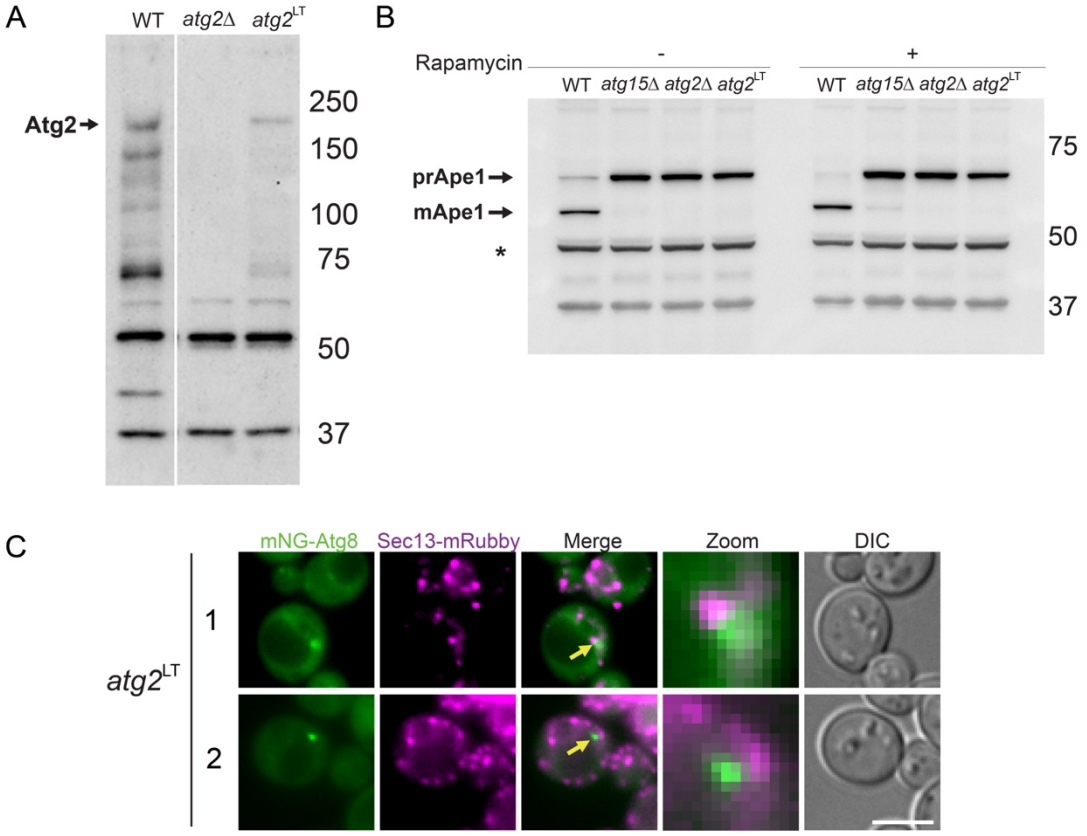

Figure S4. Construction of *atg2^{LT}* cells.

(A) Immunoblotting analysis was performed using anti-Atg2 antibodies.

(B) The same samples are used in (A). Western blot analysis was performed using an anti-Ape1 antibody. The upper bands represent precursor Ape1 (prApe1), the middle bands represent mature Ape1 (mApe1), and the lower bands represent nonspecific signals that can be used as an internal control (*).

(C) Colocalization between mNG-Atg8 and Sec13-mRubby in *atg2*^{LT} cells. The scale bar represents 5 μm.

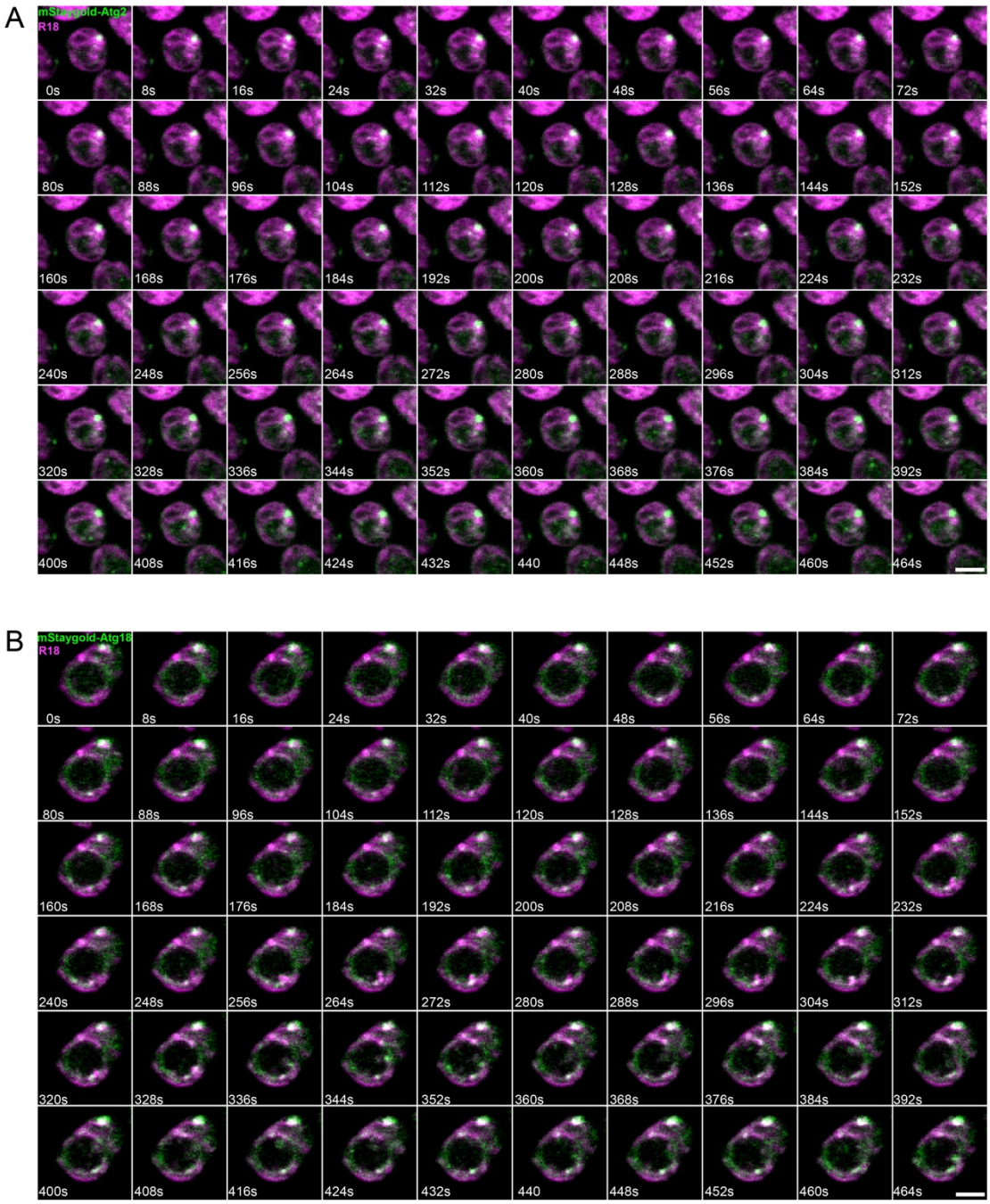

Figure S5. Localization of Atg2 and Atg18 during replenishment with nutrient-rich medium.

(A, B) Time-lapse fluorescence microscopy of yeast cells expressing mStaygold–Atg2 (A) or mStaygold–Atg18 (B) stained with the fluorescent lipid dye R18. Autophagy was induced by nitrogen starvation for 5 h and subsequently terminated by replenishment with nutrient-rich medium, under the same conditions as in Figure 5. Numbers indicate time in seconds. The scale bar represents 2 µm.

1192 **Table S1.** *S. cerevisiae* strains used in this study

1193

Strain[a]	Mat	Genotype	Source
BY4741	α	*his3Δ1 leu2Δ0 met15Δ0 ura3Δ0*	(S1)
W303-1A	α	*ade2-1 leu2-3 his3-11, 15 trp1-1 ura3-1 can1-100*	This study
SEY6210	α	*lys2 suc2 his3 leu2 trp1 ura3*	(S2)
YHL1	α	SEY6210 *atg2Δ::LEU2*	This study
YHL2	α	SEY6210 *atg15Δ::hphNT1*	This study
YHL3	α	SEY6210 *pep4Δ::LEU2*	This study
YKM674	α	SEY6210 *atg39Δ::zeoNT3 atg40Δ::hphNT1*	(S3)
YOC5565	α	SEY6210 *atg39Δ::zeoNT3 atg40Δ::hphNT1 atg15Δ::natNT2*	This study
YCK445	α	SEY6210; *DPM1-YEGFP-kanMX*	(S4)
YHL4	α	W303-1A *atg2Δ::natNT2*	This study
YHL5	α	W303-1A *atg15Δ::KANMX6*	This study
YKT38	a	*ura3-52 his3-200 trp1-63 leu2-1 lys2-801*	(S5)
YKT715	α	YKT38 *lem3Δ::TRP1*	(S6)
YKT917	α	YKT38 *dnf3Δ::HIS3MX6*	(S7)
YKT1660	a	YKT38 *KanMX6::P_{GAL1}-3HA-NEO1*	(S8)
YHL6	α	YKT38 *mNeonGreen-ATG8::LEU2*	This study
YHL9 (*atg2*^{LT})	α	YKT38 *atg2*$^{F88R\ G97S\ L180E\ L208R\ L311E}$ *mNeonGreen-ATG8::LEU2*	This study
Abp1-GFP	α	BY4741 *abp1Δ::ABP1-GFP:HIS3MX6*	(S9)
Ald6-GFP	α	BY4741 *ald6Δ::ALD6-GFP:HIS3MX6*	(S9)
Dpm1-GFP	α	BY4741 *dpm1Δ::DPM1-GFP:HIS3MX6*	(S9)
Erd2-GFP	α	BY4741 *erd2Δ::ERD2-GFP:HIS3MX6*	(S9)
Msn2-GFP	α	BY4741 *msn2Δ::MSN2-GFP:HIS3MX6*	(S9)
OM45-GFP	α	BY4741 *om45Δ::OM45-GFP:HIS3MX6*	(S9)
Pex14-GFP	α	BY4741 *pex14Δ::PEX14-GFP:HIS3MX6*	(S9)
Psr1-GFP	α	BY4741 *psr1Δ::PSR1-GFP:HIS3MX6*	(S9)
Rtn1-GFP	α	BY4741 *rtn1Δ::RTN1-GFP:HIS3MX6*	(S9)
Sec7-GFP	α	BY4741 *sec7Δ::SEC7-GFP:HIS3MX6*	(S9)
Sec61-GFP	α	BY4741 *sec61Δ::SEC61-GFP:HIS3MX6*	(S9)
Snf7-GFP	α	BY4741 *snf7Δ::SNF7-GFP:HIS3MX6*	(S9)
Tgl4-GFP	α	BY4741 *tgl4Δ::TGL4-GFP:HIS3MX6*	(S9)
Vph1-GFP	α	BY4741 *vph1Δ::VPH1-GFP:HIS3MX6*	(S9)
RY6222	α	SEY6210 *osh1Δ::URA3 osh2Δ::URA3*	(S10)
JRY6202	α	SEY6210 *osh3Δ::LYS2*	(S10)
JRY6227	α	SEY6210 *osh4Δ::HIS3 osh5Δ::LEU2*	(S10)
JRY6207	α	SEY6210 *osh6Δ::LEU2 osh7Δ::HIS3*	(S10)
CBY926	α	SEY6210 *osh1Δ::kanMX4 osh2Δ::kanMX4 osh3Δ::LYS2 osh4Δ::HIS3 osh5Δ::LEU2 osh6Δ::LEU2 osh7Δ::HIS3 osh4-1-TRP*	(S11)

ANDY201	α	SEY6210 *SEC61-GFP::TRP1 ist2Δ::HISMX6 scs2Δ::TRP1 scs22Δ::HISMX6 tcb1Δ::KANMX6 tcb2Δ::KANMX6 tcb3Δ::HISMX6*	(S12)
YTAK2095	α	YKT38 *ist2*Δ::NATMX *scs2*Δ::Hyg *scs22*Δ::KILEU2*tcb1*Δ::KanMX *tcb2*Δ::HIS3MX *tcb3*Δ::TRP1 *ice2*Δ::Aur pRS316-ER(SCS2-TM)-GFPen	This study

[a]: YKT strains are isogenic derivatives of YEF473 (S13).

Table S2. Plasmids used in this study

Name	Properties	Marker	Source
pYEX-BX[prApe1]	Plasmid for the expression of prApe1 from the *CUP*1 promoter	*URA3*	(S4)
pRS314[GFP-Atg8]	Plasmid for the expression of GFP-Atg8	*URA3*	(S14)
pRS305[mNeonGreen-Atg8]	Plasmid for the integration of mNeonGreen-Atg8	*LEU2*	(S15)
pCB255	Plasmid for the expression of *osh4-1*	*TRP1*	(S10)

1196 References

1197 S1. Brachmann, C. B. *et al*. Designer deletion strains derived from *Saccharomyces*
1198 *cerevisiae* S288C: a useful set of strains and plasmids for PCR-mediated gene
1199 disruption and other applications. *Yeast* **14**, 115–132 (1998).

1200 S2. Robinson, J. S., Klionsky, D. J., Banta, L. M. & Emr, S. D. Protein sorting in
1201 *Saccharomyces cerevisiae*: isolation of mutants defective in the delivery and
1202 processing of multiple vacuolar hydrolases. *Mol Cell Biol* **8**, 4936–4948 (1988).

1203 S3. Mochida, K. *et al*. Receptor-mediated selective autophagy degrades the
1204 endoplasmic reticulum and the nucleus. *Nature* **522**, 359–362 (2015).

1205 S4. Suzuki, K., Kubota, Y., Sekito, T. & Ohsumi, Y. Hierarchy of Atg proteins in pre-
1206 autophagosomal structure organization. *Genes to Cells* **12**, 209–218 (2007).

1207 S5. Misu, K. *et al*. Cdc50p, a Conserved Endosomal Membrane Protein, Controls
1208 Polarized Growth in Saccharomyces cerevisiae. *Mol Biol Cell* **14**, 730–747 (2003).

1209 S6. Saito, K. *et al*. Cdc50p, a protein required for polarized growth, associates with
1210 the Drs2p P-type ATPase implicated in phospholipid translocation in Saccharomyces
1211 cerevisiae. *Mol. Biol. Cell* **15**, 3418–3432 (2004).

1212 S7. Kishimoto, T. *et al*. Phospholipid flippases and Sfk1 are essential for the retention
1213 of ergosterol in the plasma membrane. *Mol Biol Cell* **32**, 1374–1392 (2021).

1214 S8. Takeda, M., Yamagami, K. & Tanaka, K. Role of Phosphatidylserine in
1215 Phospholipid Flippase-Mediated Vesicle Transport in Saccharomyces cerevisiae.
1216 *Eukaryot Cell* **13**, 363–375 (2014).

1217 S9. Huh, W. *et al*. Global analysis of protein localization in budding yeast. *Nature*
1218 **425**, 686–691 (2003).

1219 S10. Beh, C. T. & Rine, J. A role for yeast oxysterol-binding protein homologs in
1220 endocytosis and in the maintenance of intracellular sterol-lipid distribution. *Journal of*
1221 *Cell Science* **117**, 2983–2996 (2004).

1222 S11. Tian, S., Ohta, A., Horiuchi, H. & Fukuda, R. Oxysterol-binding protein
1223 homologs mediate sterol transport from the endoplasmic reticulum to mitochondria in
1224 yeast. *Journal of Biological Chemistry* **293**, 5636–5648 (2018).

1225 S12. Manford, A. G., Stefan, C. J., Yuan, H. L., Macgurn, J. A. & Emr, S. D. ER-to-
1226 plasma membrane tethering proteins regulate cell signaling and ER morphology. *Dev*
1227 *Cell* **23**, 1129–1140 (2012).

1228 S13. Longtine, M. S. et al. Additional modules for versatile and economical PCR-
1229 based gene deletion and modification in Saccharomyces cerevisiae. Yeast **14**, 953–
1230 961 (1998).

1231 S14. Suzuki, K. *et al*. The pre-autophagosomal structure organized by concerted
1232 functions of *APG* genes is essential for autophagosome formation. *EMBO J* **20**,
1233 5971–5981 (2001).

1234 S15. Hirata, E., Ohya, Y. & Suzuki, K. Atg4 plays an important role in efficient
1235 expansion of autophagic isolation membranes by cleaving lipidated Atg8 in
1236 *Saccharomyces cerevisiae*. *PLoS One* **12**, e0181047 (2017).